Hindawi

Research Article

Identification of Vibration Signal for Residual Pressure Utilization Hydraulic Unit Using MRFO-BP Neural Network

Qingjiao Cao ⓘ**, Liying Wang** ⓘ**, Jiajie Zhang, Tengfei Guo, and Xiyuan Liu**

School of Water Conservancy and Hydroelectric Power, Hebei University of Engineering, Handan, Hebei 056038, China

Correspondence should be addressed to Liying Wang; wangliying@hebeu.edu.cn

Combined with wavelet threshold denoising and Ensemble Empirical Mode Decomposition (EEMD) decomposition, an identification method based on Manta Ray Foraging Optimization-BP (MRFO-BP) neural network for vibration signals of residual pressure utilization hydraulic units is proposed to distinguish the vibration signal of each unit. The feature vectors of vibration signals are extracted by wavelet denoising and EEMD decomposition. The weights and thresholds in BP neural network are optimized by the MRFO algorithm. The feature vectors are input into the optimized BP neural network to realize the identification and classification of vibration signals. Compared with Particle Swarm Optimization-BP (PSO-BP) neural network, Bat Algorithm-BP (BA-BP) neural network, and BP neural network, the results show that the identification rate of each measuring point from the MRFO-BP neural network is greatly improved. The average identification rate of other measuring points is 98.514%, except the identification rate of the generator, which is 85.389%. Therefore, the MRFO-BP neural network has better stability and higher identification accuracy and can identify and classify vibration signals more accurately. The conclusions can provide theoretical basis for vibration signals identification of residual pressure utilization hydraulic unit. When the vibration signal of each unit cannot be clearly distinguished, the vibration signals of the units are identified by the method proposed in this paper. According to the obtained results, a feasible classification method can be provided for the vibration signals belonging to different units.

1. Introduction

The residual pressure utilization hydraulic unit is used to recover the energy wasted in the process of throttling and pressure drop and is used for residual pressure power generation, pipe network optimization, efficient pump transformation, etc. Energy saving and efficient use are realized from the two aspects of open source and reducing expenditure. Vibration phenomenon is inevitable in the operation of residual pressure utilization hydraulic unit. Most faults of the unit are reflected in the vibration signal, so the vibration signal of the unit can directly reflect whether the unit runs safely and stably [1, 2]. Comprehensive, accurate, and effective identification of vibration signals is the premise of unit condition monitoring, and it is necessary to judge the stable operation of residual pressure utilization hydraulic unit [3].

In the identification of the vibration signal of the unit, the feature vector extraction of the signal is an indispensable part. In recent years, many scholars have proposed different methods in signal feature vector extraction and recognition combined with optimization algorithms. In order to promote the effect of variational mode decomposition (VMD), Li et al. [4] proposed a feature extraction method based on GA-VMD and center frequency for the difficulty of bearing fault feature extraction. In order to improve the ability of SlEn to distinguish different types of signals and solve the problem of two threshold parameters selection, Li et al. [5] proposed a new time series complexity indicator on the basis of SlEn by introducing fractional calculus and combining particle swarm optimization (PSO), named PSO fractional SlEn (PSO-FrSlEn). Aiming at the feature extraction and identification algorithm of AE signal for fatigue crack of pipeline structure, Wei et al. [6] proposed a fatigue crack

identification method based on PNN combined with EMD feature extraction. In order to obtain short-term accurate power generation prediction, Hou et al. [7] used the Grey Wolf Optimization Algorithm (GWO) to optimize the initial weights and initial thresholds of the BP network. In order to predict the rock mass parameters of the TBM tunnel, Liu B. et al. [8] proposed a hybrid algorithm (SA-BPNN), which integrated the backpropagation neural network (BPNN) with simulated annealing (SA). Lee and Cheng [9] proposed a motor fault detection method based on wavelet transform (WT) and improved PSO-BP neural network for motor fault detection. Deepti Deshwal et al. [10] used hybrid robust feature extraction techniques for spoken language identification (LID) system and used forward backpropagation neural network (FFBPNN) for language identification or classification. Houssein et al. [11] proposed a new hybrid ECG arrhythmia classification method combining Manta Ray Foraging Optimization algorithm (MRFO) and Support Vector Machine (SVM). Yousri et al. [12] proposed a re-combination and optimization method of the electrical photovoltaic array based on the Artificial Ecosystem-based Optimization (AEO) to solve the problem of harvesting the maximum power from a partially shaded photovoltaic array. Abdolrasol et al. [13] enhanced the neural network by optimizing the algorithm and obtained the best structural network pattern by manipulating its tuned parameters or training parameters. This paper includes some results of PSO, GA, ABC, and BSA optimization techniques to improve the performance of neural network. Xiong et al. [14] proposed a novel application based on Supply-Demand-based Optimization (SDO) to extract accurate and reliable parameters for photovoltaic models. In order to study the optimal control and operation of the power distribution system, Elattar et al. [15] applied the MRFO algorithm to IEEE 33-bus, 69-bus, and practical distribution network of 84-bus in the Taiwan Power Company (TPC). The results show that the MRFO algorithm is more effective and robust than other optimization techniques. Almagboul et al. [16] proposed a novel partially connected hybrid analog-digital receive beamformer based on the Atom Search Optimization algorithm (ASO), which is used to reduce the peak sidelobe level (SLL) and steer the nulls in the desired directions. Zhang and Li [17] used Particle Swarm Optimization (PSO) to optimize the BP neural network and used the trained neural network to predict the fault arc. Ismail et al. [18] coupled the PSO and BP algorithms and applied the algorithm to predict the load-deformation behavior of axially loaded piles, and the results showed that the proposed algorithms are more accurate than others. Shadman Abid et al. [19] solved the problem of RDG planning optimization by using Artificial Hummingbird Algorithm (AHA). Tharwat et al. [20] proposed Bat Algorithm (BA) to optimize the parameters of SVM, and the results of the BA-SVM algorithm are compared with those of the grid search, which is a conventional method of searching parameter values, and two well-known optimization algorithms (GA and PSO), and the results showed that the proposed model can find the optimal values of the SVM parameters.

In view of the nonlinear, nonstationary, and strong noise characteristics of the vibration signal of the unit, wavelet threshold denoising is used to denoise the vibration signal [21], which can suppress the noise interference and protect the useful information from being lost to the greatest extent. Vamsi et al. [22] used vibration data to monitor the damage of pultruded samples, and wavelet transform was used to process the vibration signals of healthy samples and damaged samples. The Empirical Mode Decomposition (EMD) method does not need to set the wavelet basis function and the number of decomposition layers, so it is widely used in the field of processing nonlinear and nonstationary signals [23]. However, the EMD method has problems such as insufficient endpoint effect and obvious modal aliasing. Wu and Huang [24] proposed an Ensemble Empirical Mode Decomposition (EEMD). Adding Gaussian white noise to the signal to be measured can effectively reduce the problems of the EMD. Sun [25] researched the fault signal extraction and identification of vibration motor rolling bearings, and the results proved that EEMD is obviously stronger than EMD. The vibration signals are decomposed into Intrinsic Mode Function (IMF) components by EEMD. He et al. [26] used EEMD method to extract features of vibration signals of hydropower units, which verified the feasibility of this method for feature extraction of vibration signals.

The advantages of manta ray foraging optimization algorithm (MRFO) are that it does not need to provide an accurate mathematical optimization model, and the optimization method of the objective function and constraint function is more relaxed. At the same time, it has strong global search ability and is not restricted by functions and continuous factors. When running the MRFO algorithm, it has the characteristics of strong optimization ability, fast convergence, and few parameters [27]. For the problems of unreasonable selection of initial weights and thresholds, poor network convergence, and prediction accuracy in BP neural network [7], MRFO algorithm can be used to optimize BP neural network. Therefore, combined with wavelet threshold denoising and EEMD [28, 29] feature extraction method, an analysis method named MRFO-BP neural network, which is based on the MRFO algorithm and BP neural network, is proposed to extract and identify the vibration signal features of residual pressure utilization hydraulic unit. The vibration signal is denoised by the wavelet threshold denoising method, and then the denoising vibration signal is decomposed by the EEMD method. The IMF components are extracted as the feature vectors and input into the optimized BP neural network for vibration signals identification. The MRFO-BP neural network is compared with PSO-BP neural network, BA-BP neural network, and BP neural network. The results show that the identification rate of MRFO-BP neural network is higher, and it can more effectively distinguish the vibration signals of different units in the same position. This method can provide a theoretical basis for the subsequent identification of the vibration signals of residual pressure utilization hydraulic unit.

2. Experiment and Signal Processing

2.1. Experiment. The experimental data are the vibration signals collected by the residual pressure utilization hydraulic units of industrial fluid in a chemical company in Henan Province. The units are shown in Figure 1. There are five similar units, and the capacity is 200 kW. The runner is HL360A, and the speed is 600 r/min. Three units (1#, 3#, and 4#) are selected as the vibration test objects. The shaft of the 1# unit is shattered and just repaired. The 4# unit is running well. Compared with the 4# unit, the noise of the 3# unit is too big. The acceleration sensors are set in five parts of each unit as the measuring points, and the vertical and horizontal directions are arranged in coordination, as shown in Figures 2–4. The five measuring points are the generator, the inlet, the middle of the spiral casing, the tail of the spiral casing, and the outlet. The 10 measuring points are numbered from No. 1 to No. 10, respectively. The guide vanes opening of the units are selected as 40 mm.

DASP-V10 vibration data acquisition instrument is used to collect vibration signals. Ten models of INV9828 piezoelectric acceleration sensors are selected. The sampling frequency of vibration signal is 1024 Hz. The basic parameters of the acceleration sensors are shown in Table 1.

The experimental data of three residual pressure utilization hydraulic units are divided into five categories according to the different positions of measuring points. The specific classification is shown in Table 2. The three cases of each category are classified as 1# unit number 1, 3# unit number 2, and 4# unit number 3.

2.2. Feature Extraction Method. The vibration frequency distribution of Gaussian white noise is uniform, which can effectively reduce the problem of insufficient endpoint effect and suppress the phenomenon of modal aliasing [30]. Based on the original EMD method, the EEMD method is proposed, which is realized by adding white noise with equal amplitude to the original signal for many times, and using EMD to decompose the signal after adding white noise [31, 32]. In order to reduce the influence of white noise on the signal to be measured, the average value of the IMF components obtained by EMD decomposition is used as the final decomposition result.

The EEMD method is selected to extract the features of the vibration signals of the residual pressure utilization hydraulic unit. Firstly, the wavelet threshold denoising method is applied to denoise the original signal, and then the denoised vibration signals are decomposed by the EEMD method, and the IMF components are extracted as the feature vectors to input the optimized BP neural network to identify the vibration signals. The feature vectors extraction process of the vibration signals is shown in Figure 4.

2.3. Vibration Signal Processing and Feature Extraction. The wavelet threshold denoising method is used to denoise the vibration signals, and the "db1" wavelet function is selected, with three decomposition layers. Taking the vibration signals at the inlet of the three units as an example,

the comparison waveform of the vibration signals before and after denoising is shown in Figure 5, with the abscissa as the sampling points and the ordinate as the amplitude (/mm). It can be seen from Figure 5 that the original vibration signals are disturbed by external noise, and feature extraction of the denoised signals can improve the accuracy of signal identification. The denoised vibration signals are decomposed by EEMD, and the IMF components are obtained as shown in Figure 6.

In order to unify the dimensions of the feature vectors, the feature vectors of different dimensions are substituted into the MRFO-BP neural network. After many times of training, IMF7–IMF12 are finally selected as the feature vector $X = [X_1, X_2, X_3, X_4, X_5, X_6]$ of each group of vibration signals.

3. Establishment of the MRFO-BP Neural Network Identification Model

3.1. Manta Ray Foraging Optimization. The manta ray foraging optimization algorithm is a new intelligent bionic swarm algorithm proposed by Zhao et al. [33] in 2020. Manta rays are large marine creatures. They usually appear in groups when foraging, and they feed on plankton with uneven or irregular distribution. Figure 7 depicts a foraging manta ray. The manta ray foraging optimization algorithm is a bionic optimization algorithm, which is inspired by the intelligent foraging strategy of manta ray. Manta rays usually appear in groups when foraging, and they have evolved a set of intelligent foraging strategies. The MRFO algorithm is obtained by mathematically modeling of the three predation strategies of manta rays.

The MRFO algorithm searches for the optimal solution in the space by imitating chain foraging, spiral foraging, and flipping foraging behaviors of manta rays and achieves global optimization [34]. The first is chain foraging, in which the manta ray groups will line up one after the other. This arrangement is conducive to the former manta ray missing food, and the subsequent manta ray to make up for the former's mistake. The second is spiral foraging. When the manta rays detect that the food concentration is very high, the manta ray groups will gather together and connect their tails with their heads in a spiral shape, thus forming a spiral apex, and the filtered water will move up to the surface of the water. This will pull plankton into their open mouths. The third is flip foraging, which is an uncommon foraging behavior, but an extremely effective strategy. When the manta rays detect food, the manta rays will perform a series of random, frequent backflips centered on the food.

3.1.1. Chain Foraging. During foraging, manta rays can observe the position of plankton and swim toward it, with the higher concentrations of plankton indicating the better location. Assuming that the position of high concentrations plankton indicates the optimal position, manta rays are connected end to end in a feeding chain. The first manta ray swims toward the optimal position, and the other manta rays swim not only toward the optimal position, but also toward

FIGURE 1: Test units.

FIGURE 3: Measuring point layout of the residual pressure utilization hydraulic unit.

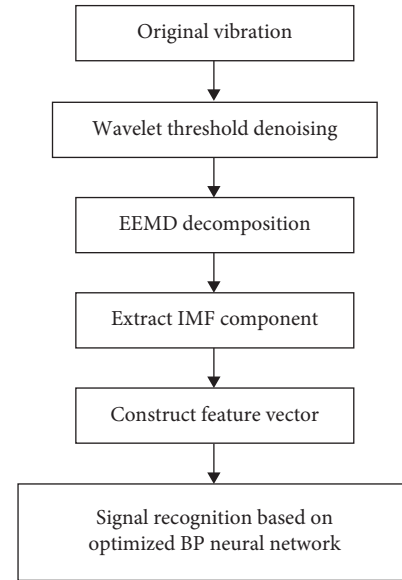FIGURE 2: Measuring point layout of the generator.

FIGURE 4: Feature extraction process based on EEMD.

the position of the previous manta ray. So, during the iteration process, each manta ray updates its position according to the current global optimal position and the previous individual position. The individual position update is given by the following equation:

$$
x_i^{\mathrm{d}}(t+1) = \begin{cases} x_i^{\mathrm{d}}(t) + r \cdot \left(x_{\mathrm{best}}^{\mathrm{d}}(t) - x_i^{\mathrm{d}}(t) \right) \\ \quad + \alpha \cdot \left(x_{\mathrm{best}}^{\mathrm{d}}(t) - x_i^{\mathrm{d}}(t) \right), \quad i = 1, \\ x_i^{\mathrm{d}}(t) + r \cdot \left(x_{i-1}^{\mathrm{d}}(t) - x_i^{\mathrm{d}}(t) \right) \\ \quad + \alpha \cdot \left(x_{best}^{\mathrm{d}}(t) - x_i^{\mathrm{d}}(t) \right), \quad i = 2, \ldots, N, \end{cases} \tag{1}
$$

$$
\alpha = 2 \cdot r \cdot \sqrt{|\log(r)|}, \tag{2}
$$

TABLE 1: Basic parameter table of the acceleration transducer.

Position	Measuring point	Model	Types	Direction	Unit EU	Sensitivity mV/EU	Data channel
Generator	1	INV9828	Acceleration	X	mm/s2	50.220	2
	2	INV9828	Acceleration	Y	mm/s2	49.490	1
Inlet	3	INV9828	Acceleration	X	mm/s2	48.030	4
	4	INV9828	Acceleration	Y	mm/s2	50.510	3
Middle of the spiral casing	5	INV9828	Acceleration	X	mm/s2	50.530	12
	6	INV9828	Acceleration	Y	mm/s2	49.595	11 (9)1
Tail of the spiral casing	7	INV9828	Acceleration	X	mm/s2	49.422	6
	8	INV9828	Acceleration	Y	mm/s2	50.510	5
Outlet	9	INV9828	Acceleration	X	mm/s2	46.660	7
	10	INV9828	Acceleration	Y	mm/s2	49.386	8

In the experiment of measuring point 6, channel 11 is selected for 1# unit, channel 9 is selected for 3# unit and 4# unit, and the other parameters are completely the same.

TABLE 2: Classification of experimental data.

Measuring point position	Unit	Experimental point	Direction	Category label
Generator	1# unit	1	X	1
		2	Y	
	3# unit	1	X	2
		2	Y	
	4# unit	1	X	3
		2	Y	
Inlet	1# unit	3	X	1
		4	Y	
	3# unit	3	X	2
		4	Y	
	4# unit	3	X	3
		4	Y	
Middle of the spiral casing	1# unit	5	X	1
		6	Y	
	3# unit	5	X	2
		6	Y	
	4# unit	5	X	3
		6	Y	
Tail of the spiral casing	1# unit	7	X	1
		8	Y	
	3# unit	7	X	2
		8	Y	
	4# unit	7	X	3
		8	Y	
Outlet	1# unit	9	X	1
		10	Y	
	3# unit	9	X	2
		10	Y	
	4# unit	9	X	3
		10	T	

where t and d represent the number of iterations and dimension, respectively. $x_i^d(t)$ represents the individual position of the i generation. r represents a random number in the range of $[0, 1]$. $x_{best}^d(t)$ represents the best position. α represents weight coefficient.

3.1.2. Spiral Foraging.
When the plankton is found in the deep water, the manta ray will move towards the food in a spiral form, and the individual manta ray will also follow the previous individual to update the position. The position update equation is as follows:

$$x_i^d(t+1) = \begin{cases} x_{best}^d(t) + r \cdot \left(x_{best}^d(t) - x_i^d(t)\right) \\ + \beta \cdot \left(x_{best}^d(t) - x_i^d(t)\right), \quad i = 1, \\ x_{best}^d(t) + r \cdot \left(x_{i-1}^d(t) - x_i^d(t)\right) \\ + \beta \cdot \left(x_{best}^d(t) - x_i^d(t)\right), \quad i = 2, \ldots, N, \end{cases} \quad (3)$$

$$\beta = 2 \cdot e^{r_1 \cdot T - t + 1/T} \cdot \sin\left(2 \cdot \pi \cdot r_1\right), \quad (4)$$

where β represents the spiral weight coefficient. T represents the maximum number of iterations. r_1 represents a random

number in the range of $[0, 1]$. Formula (3) indicates that the MRFO algorithm searches near the optimal solution in the n-dimensional space and has good local search ability.

The individual manta ray uses the food position as the reference position to search randomly, which can improve the global search ability of the algorithm and avoid falling into the local optimization. The expression is as follows:

$$x_{\text{rand}}^{\text{d}} = Lb^{\text{d}} + r \cdot \left(Ub^{\text{d}} - Lb^{\text{d}}\right), \tag{5}$$

$$x_i^{\text{d}}(t+1) = \begin{cases} x_{\text{rand}}^{\text{d}}(t) + r \cdot \left(x_{\text{rand}}^{\text{d}} - x_i^{\text{d}}(t)\right) \\ + \beta \cdot \left(x_{\text{rand}}^{\text{d}}(t) - x_i^{\text{d}}(t)\right), \quad i = 1, \\ x_{\text{rand}}^{\text{d}}(t) + r \cdot \left(x_{i-1}^{\text{d}}(t) - x_i^{\text{d}}(t)\right) \\ + \beta \cdot \left(x_{\text{rand}}^{\text{d}}(t) - x_i^{\text{d}}(t)\right), \quad i = 2, \ldots, N, \end{cases} \tag{6}$$

where $x_{\text{rand}}^{\text{d}}(t)$ represents a random position randomly generated by the individual in the search space. Ub^{d} and Lb^{d} represent the upper and lower limits of the value, respectively.

3.1.3. Flip Foraging.

In the flipping foraging behavior, the manta rays flip to a new position with the food position as the fulcrum. The new position is any position in the search domain between the current position and the symmetrical position of the best position it has found so far. In the search space, as the distance between the individual position and the best position found so far decreases, all individuals gradually approach the optimal solution. The expression is as follows:

$$x_i^{\text{d}}(t+1) = x_i^{\text{d}}(t) + S \cdot \left(r_2 \cdot x_{\text{best}}^{\text{d}} - r_3 \cdot x_i^{\text{d}}(t)\right), \quad i = 1, \ldots, N, \tag{7}$$

where S represents the flip factor of the manta rays flip range. The size of S determines the individual flip distance of the manta rays. This paper takes $S = 2$. r_2 and r_3 represent random numbers in $[0, 1]$.

3.2. Optimization of BP Neural Network by MRFO Algorithm.

The BP neural network [35] is a feed-forward neural network algorithm that conducts backward transmission training with error. It consists of input layer, hidden layer, and output layer, including feed-forward calculation process and error backpropagation process [36]. BP neural network is introduced to identify and classify the feature vectors obtained by EEMD decomposition.

Aiming at the unavoidable problems of BP neural network, such as easily falling into local minimum, slow convergence speed, and weak generalization ability, the MRFO algorithm is used to optimize BP neural network. The random initial population individuals within the boundary range are used as neural network parameters to assign initial values to the weights and thresholds of the network. Then, the BP neural network is used as the fitness function, and the calculated error is used as the fitness value. The population individuals and fitness values are continuously updated

through the MRFO algorithm. After many iterations, the optimal population individual and the global optimal fitness value are obtained. The optimal population individuals are substituted into the BP neural network to update the weights and thresholds, and the identification results of the residual pressure utilization hydraulic unit vibration signals are calculated. The identification process of MRFO-BP neural network is shown in Figure 8. The specific description is as follows:

Step 1. Parameter initialization. Set the population size N, the maximum iteration number T, and the number of nodes in each layer of BP neural network;

Step 2. Population initialization. Randomly initial population individuals, using the BP neural network as the fitness function to calculate the individual fitness value;

Step 3. Generate a random number R_1;

Step 4. If $R_1 \geq 0.5$, update the position according to Equation (1); otherwise, generate a random number R_2;

Step 5. If $R_2 < t/T$, update the position according to Equation (3); otherwise, update the position according to Equation (6);

Step 6. Calculate the updated fitness value, and then update the position according to Equation (7);

Step 7. Update the population and the global optimal position;

Step 8. Judge whether the algorithm meets the termination condition. If so, output the optimal model of the BP neural network to identify the vibration signals. Otherwise, return to Step 3.

3.3. Training MRFO-BP Neural Network.

The parameters of MRFO-BP neural network are initialized: the initial population number is 30, the maximum number of iterations is 200, the number of nodes in the input layer is 6, the number of nodes in the hidden layer is 10, and the number of nodes in the output layer is 3.

Six groups of signals at the inlets of three units, each with 1000 IMF7-IMF12 components, are selected as the feature vectors of the vibration signals of residual pressure utilization hydraulic units. The feature vector sets are input into the MRFO-BP neural network for training and prediction. For each group of signals, the first 700 pieces of data are selected as training data, and the remaining 300 pieces of data are selected as the test data. The data are normalized to form a sample set. The training data set and initialization parameters are input into MRFO-BP neural network. After the BP neural network training and MRFO algorithm optimization, the optimal population and global optimal fitness value are obtained. The historical optimal fitness value curve of the inlet in the target space is shown in Figure 9.

It can be seen from Figure 9 that the initial fitness value at the inlet of the unit is 9084.238, which is maintained until the 12th iteration. The changes of the fitness value in the intermediate iteration process are as follows: the 13th to
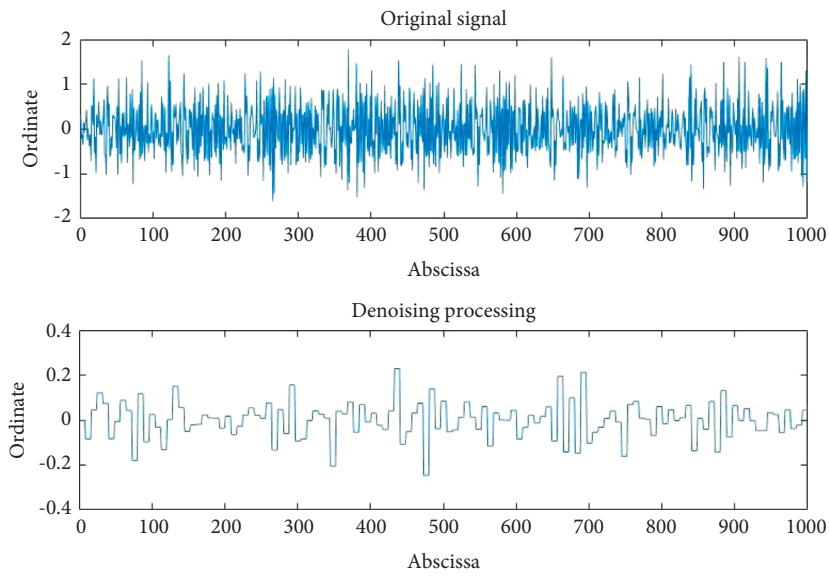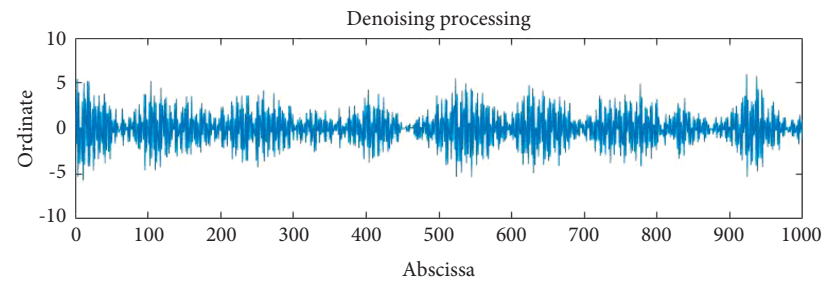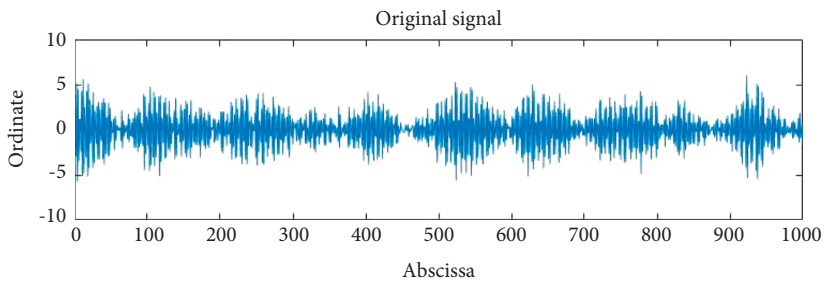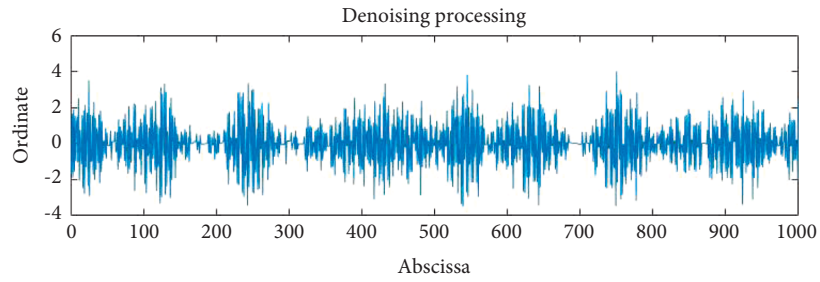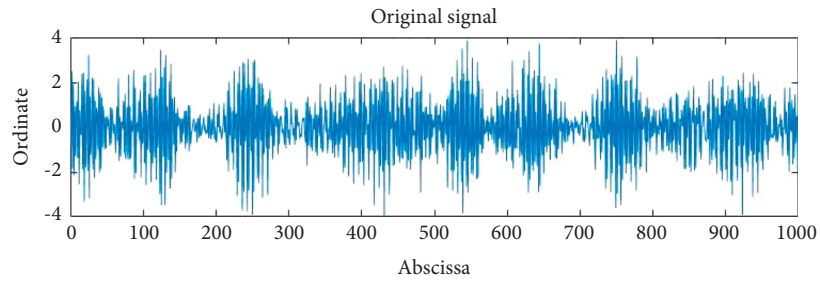
(a)
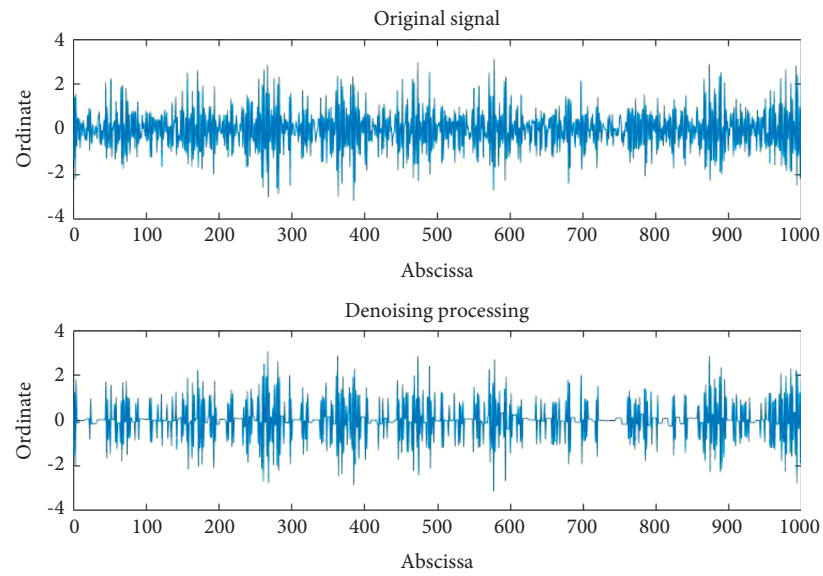
(b)

FIGURE 5: Continued.

(c)
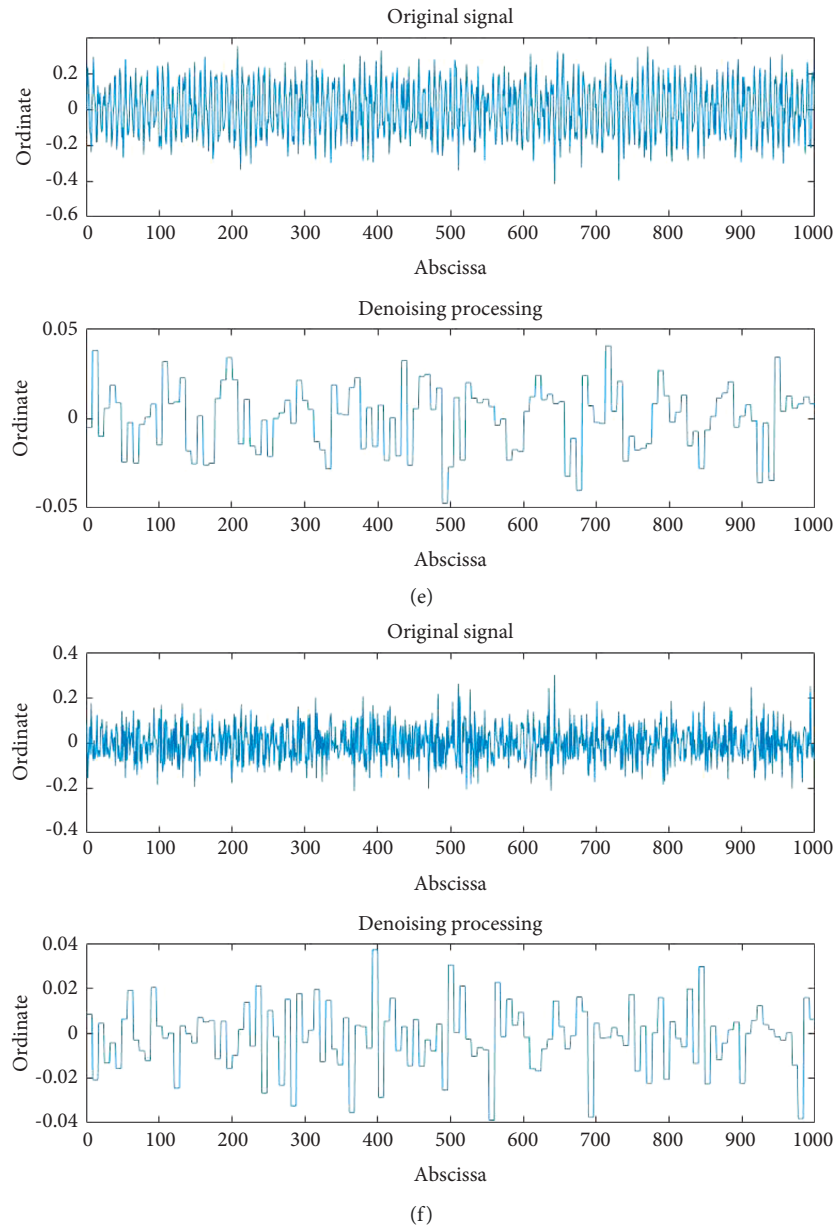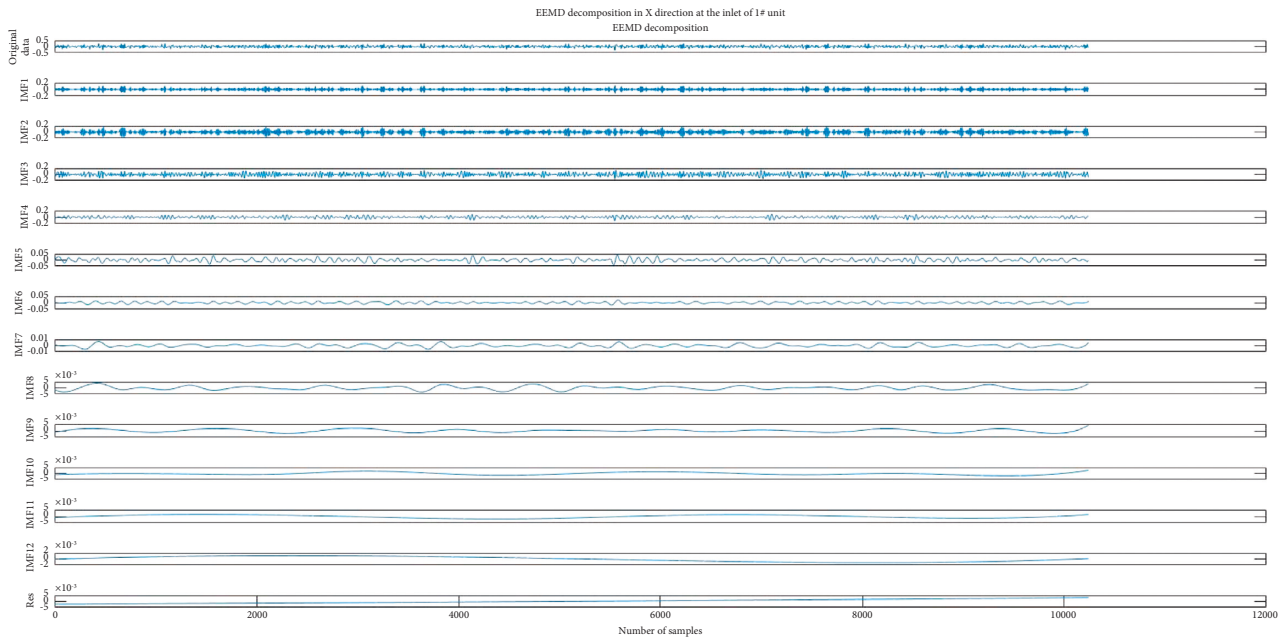

(d)

Figure 5: Continued.

FIGURE 5: Contrast waveform of vibration signals before and after denoising. (a) *X* direction at the inlet of 1# unit; (b) *Y* direction at the inlet of 1# unit; (c) *X* direction at the inlet of 3# unit; (d) *Y* direction at the inlet of 3# unit; (e) *X* direction at the inlet of 4# unit; (f) *Y* direction at the inlet of 4# unit.

103rd iterations are 8630.783, and the 104th to 179th iterations are 8408.997. At the 180th iteration, the optimal fitness value is 8400.970.
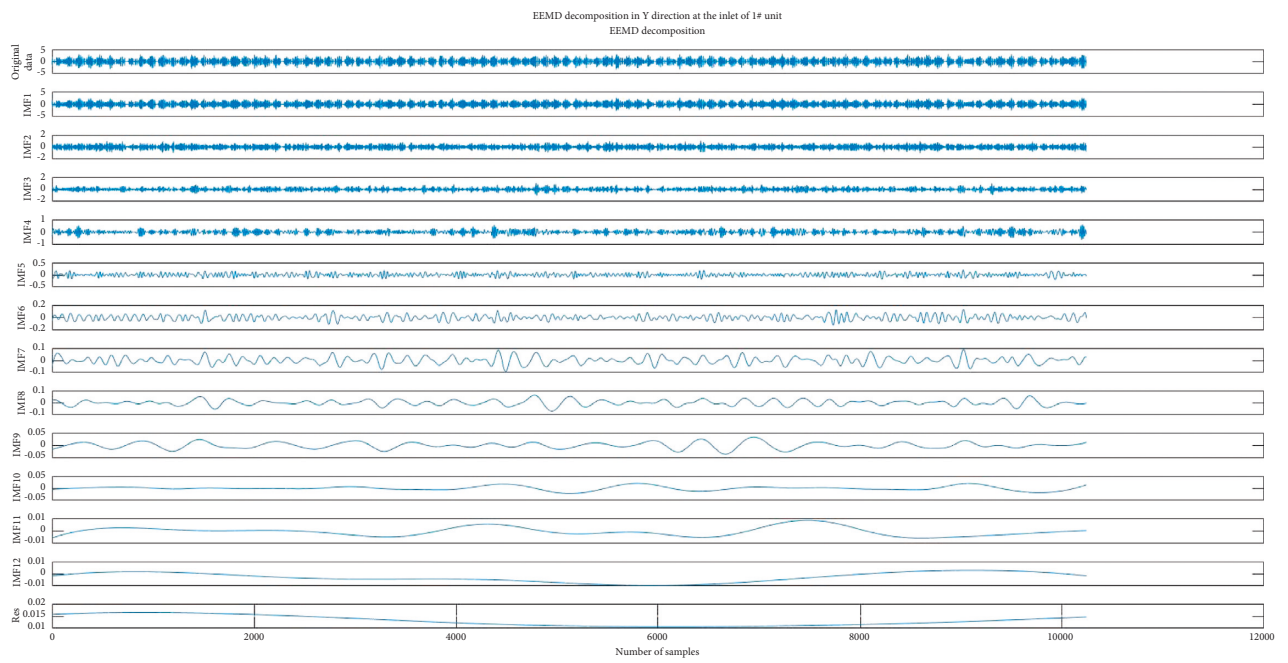
The vibration signals of the generator, the middle of the spiral casing, the tail of the spiral casing, and the outlet of the three residual pressure utilization hydraulic units are substituted into the MRFO-BP neural network, and the optimal population and global optimal fitness values are obtained, respectively. The historical optimal fitness value curve of each measuring point in the target space is shown in Figures 10–13.

It can be seen from Figure 10 that the initial fitness value at the generator of the unit is 8400.116, which is maintained until the 6th iteration. The fitness value is 8400.061 from the 7th to the 117th iteration. At the 118th iteration, the optimal fitness value is 8400.034.

It can be seen from Figure 11 that the initial fitness value in the middle of the spiral casing of the unit is 8818.357, which is maintained until the second iteration. The changes of the fitness value in the intermediate iteration process are as follows: the 3rd to 42nd iterations are 8401.040, the 43rd to 49th iterations are 8400.524, the
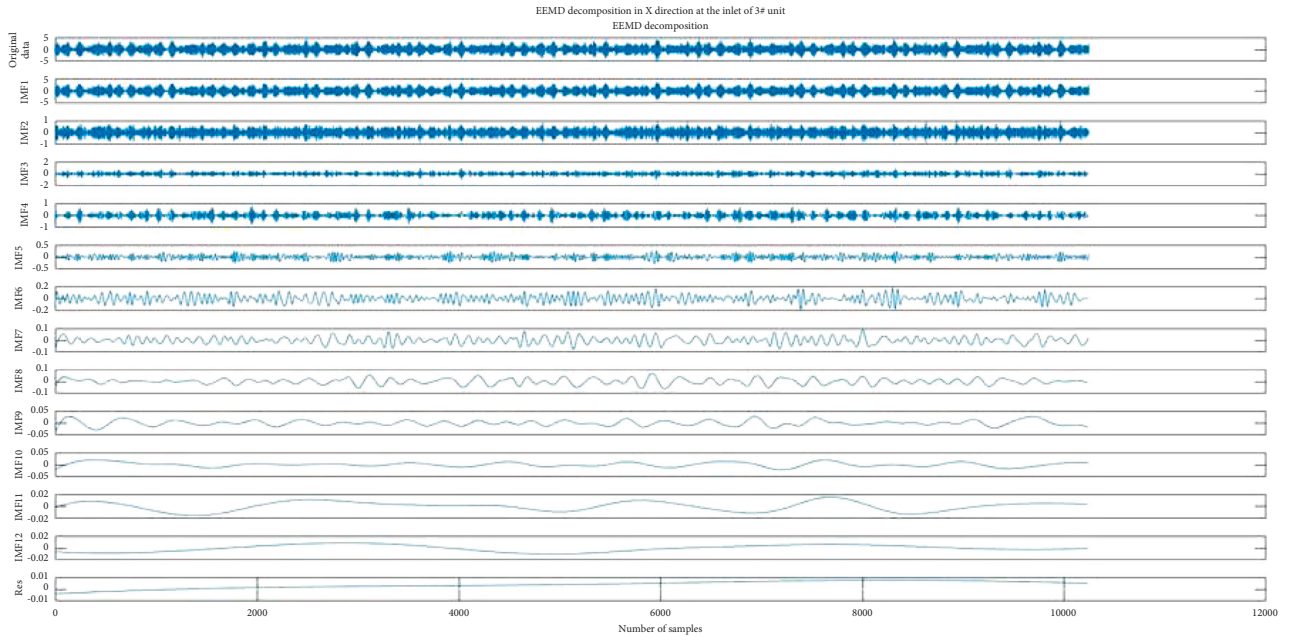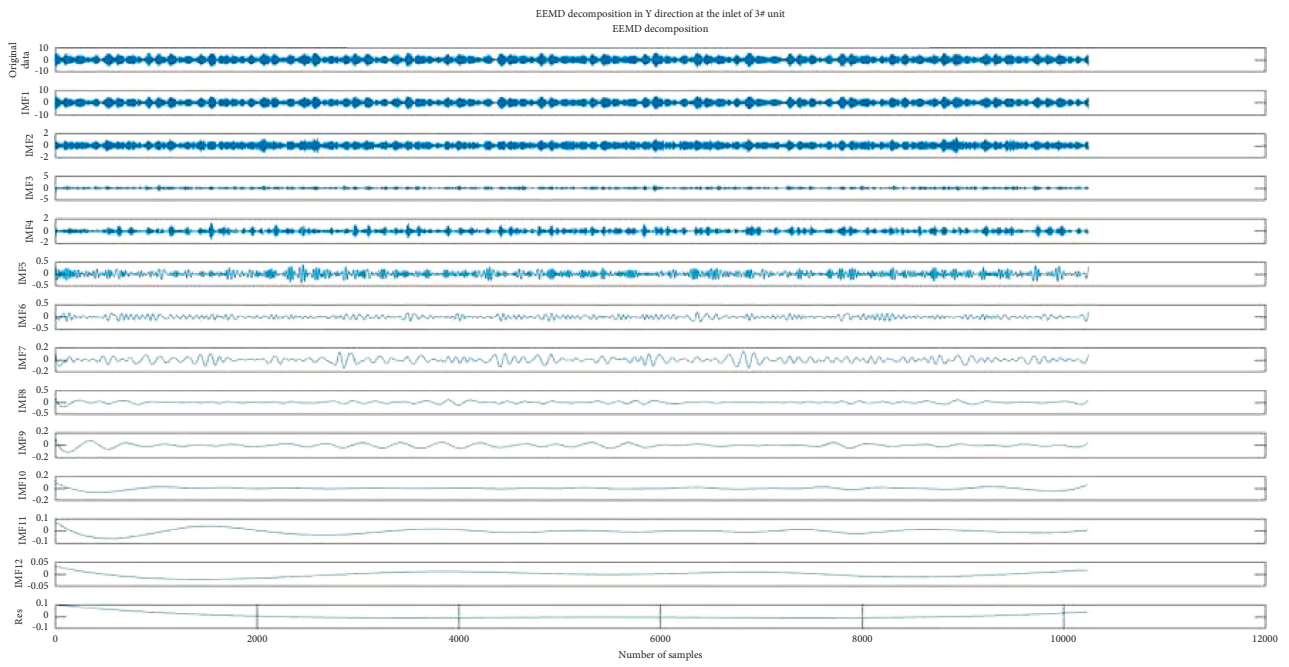
(a)

(b)

Figure 6: Continued.

EEMD decomposition in X direction at the inlet of 3# unit
EEMD decomposition

(c)

EEMD decomposition in Y direction at the inlet of 3# unit
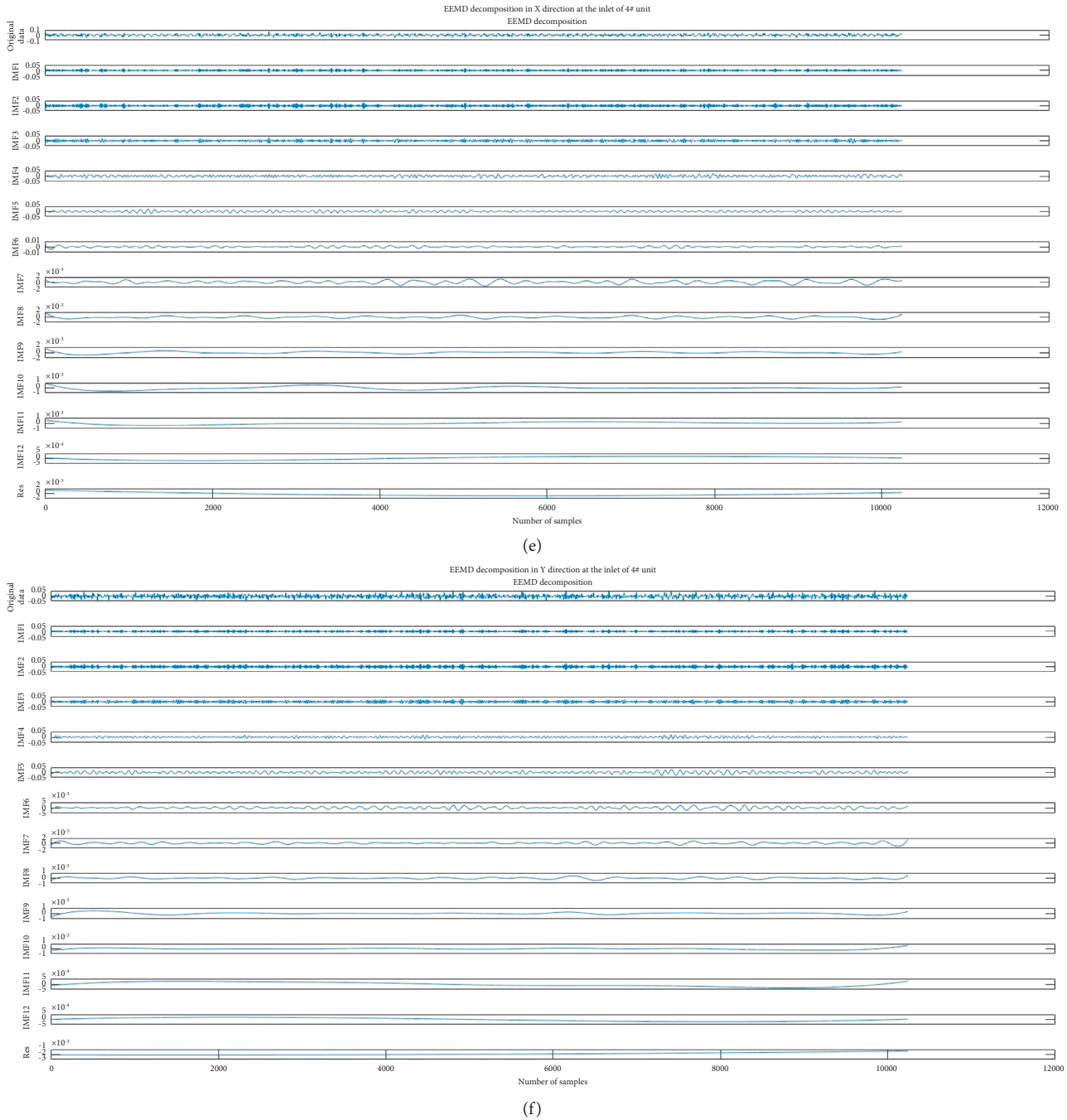EEMD decomposition

(d)

FIGURE 6: Continued.

(e)

(f)

Figure 6: Decomposition waveform of vibration signal after denoising by EEMD. (a) *X* direction at the inlet of 1# unit; (b) *Y* direction at the inlet of 1# unit; (c) *X* direction at the inlet of 3# unit; (d) *Y* direction at the inlet of 3# unit; (e) *X* direction at the inlet of 4# unit; (f) *Y* direction at the inlet of 4# unit.

50th to 73rd iterations are 8400.406, the 74th to 101st iterations are 8400.167, the 102nd iteration is 8400.165, and the 103rd to 149th iterations are 8400.146. At the 150th iteration, the optimal fitness value is 8400.071.

It can be seen from Figure 12 that the initial fitness value in the tail of the spiral casing of the unit is 8400.506, which is maintained until the 7th iteration. The changes of the fitness value in the intermediate iteration process are as follows: the

8th to 27th iterations are 8400.380, the 28th to 67th iterations are 8400.351, and the 68th to 72nd iterations are 8400.250. At the 73rd iteration, the optimal fitness value is 8400.072.

It can be seen from Figure 13 that the initial fitness value at the outlet of the unit is 8475.034. The changes of the fitness value in the intermediate iteration process are as follows: the 2nd to 3rd iterations are 8401.308, the 4th

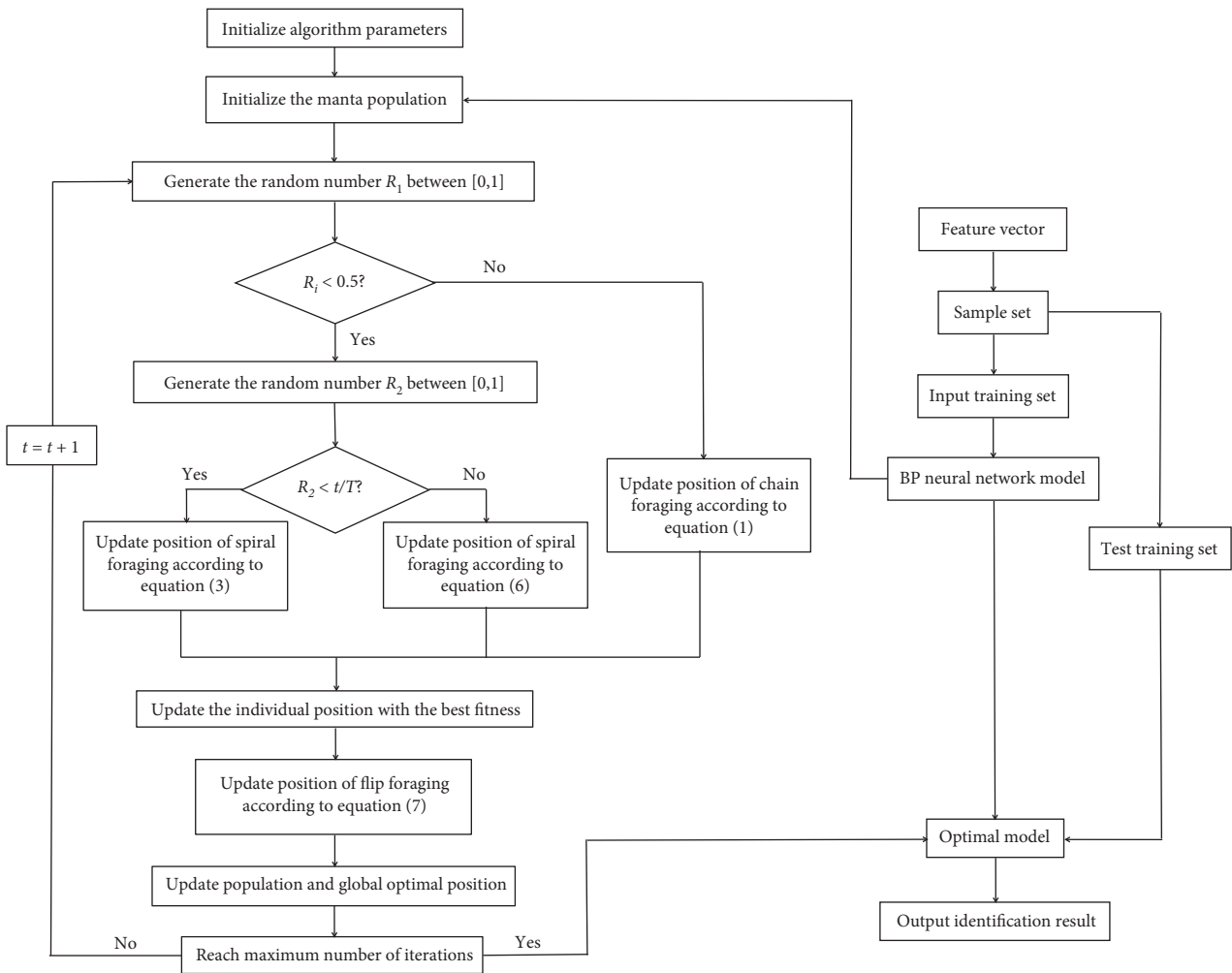FIGURE 7: A foraging manta ray.

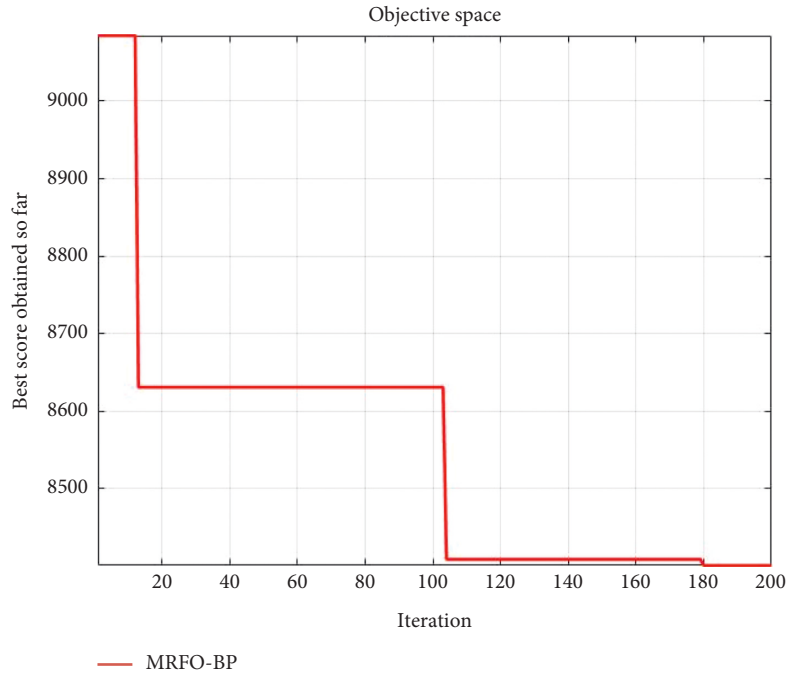FIGURE 8: Flow chart of MRFO-BP neural network identification.

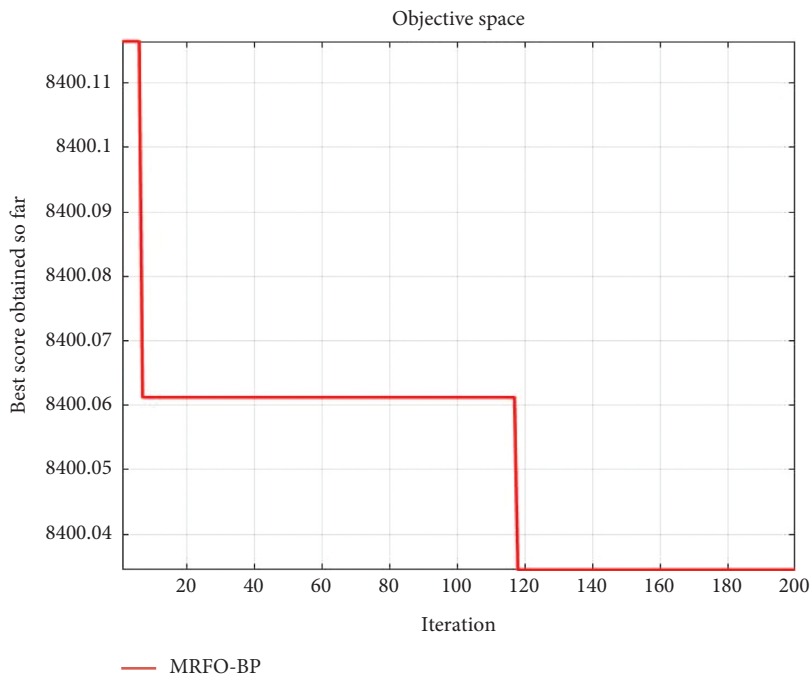FIGURE 9: Historical optimal position curve of the inlet.

FIGURE 10: Historical optimal position curve of the generator.

to 8th iterations are 8400.684, the 9th to 26th iterations are 8400.309, the 27th to 124th iterations are 8400.160, the 125th to 175th iterations are 8400.151, and the 176th to 178th iterations are 8400.106. At the 179th iteration, the optimal fitness value is 8400.072.

3.4. MRFO-BP Neural Network Identification. The weights and thresholds of the BP neural network are optimized by using the optimal population. Then, 1000 pieces of data for each of the 6 groups of signals at the inlet of the three residual pressure utilization hydraulic units are divided into
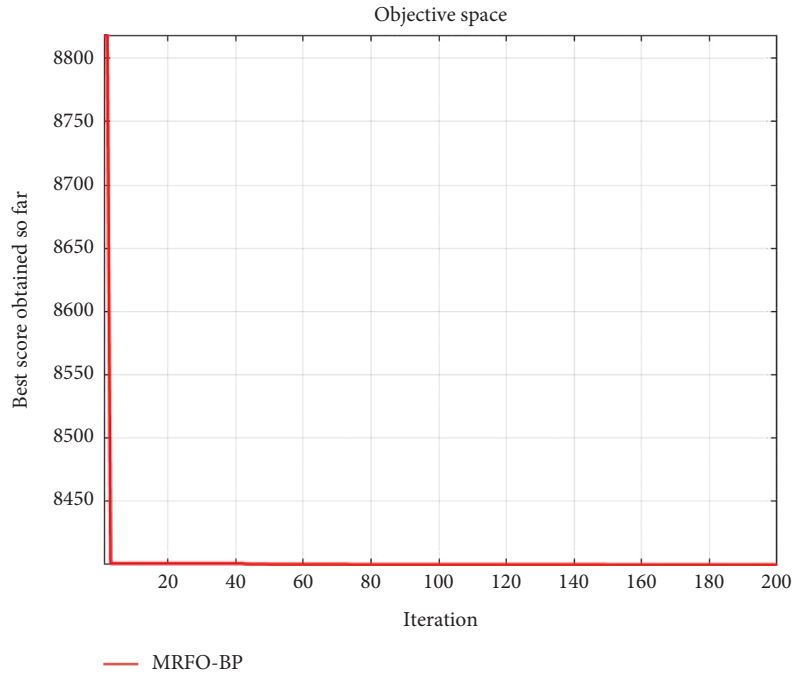
Objective space

FIGURE 11: Historical optimal position curve of the middle of the spiral casing.
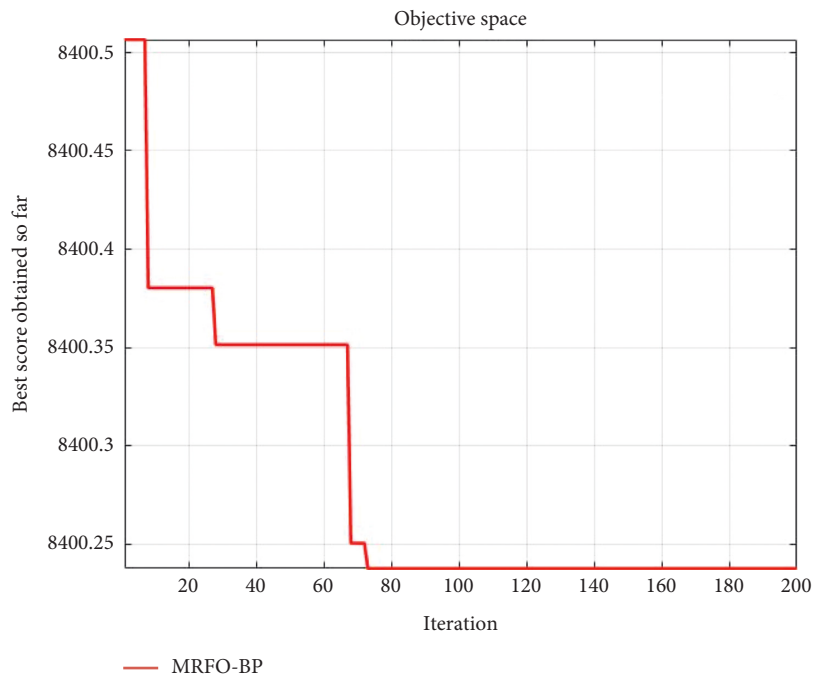
Objective space

FIGURE 12: Historical optimal position curve of the tail of the spiral casing.

the first 700 data as training data and the remaining 300 data as test data, which are, respectively, input into the BP neural network. After training and prediction, the identification rate of vibration signals is obtained through comparing the prediction results with each group of classification labels. In the MRFO-BP neural network, the identification rate of the three units at the inlet is 99.167%, and the image of the identification rate is shown in Figure 14.

In Figure 14, at the inlet, the 600 predicted values of the 1# unit completely coincide with the marker 1, the 600 predicted values of the 4# unit completely coincide with the marker 3, and the probability that the 600 predicted values of the 3# unit do not coincide with the marker 2 is 0.833%.

Objective space
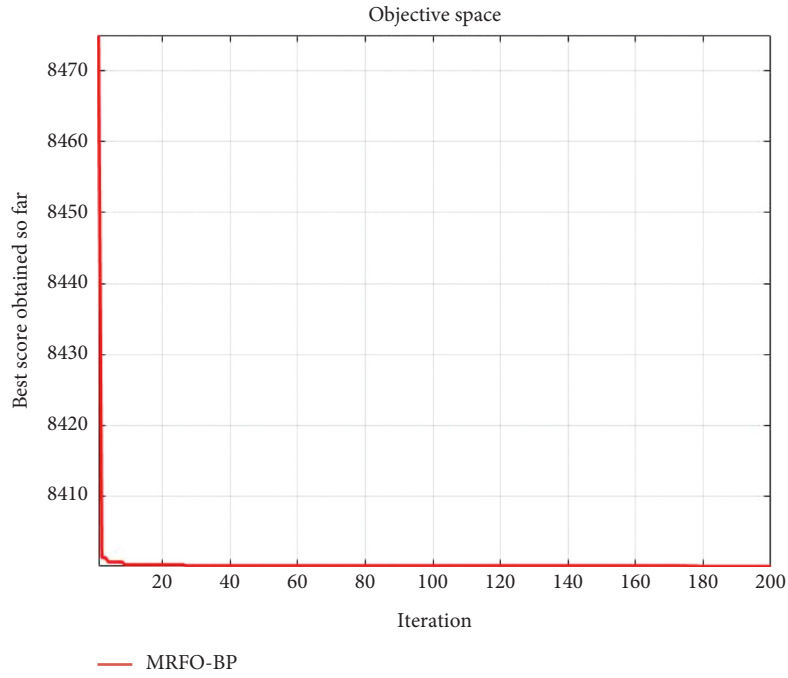
FIGURE 13: Historical optimal position curve of the outlet.

Classification results of vibration signals

FIGURE 14: Identification rate of the inlet based on MRFO-BP neural network.

TABLE 3: Identification rates of three units based on MRFO-BP neural network.

Measuring point position	Generator (%)	Middle of the spiral casing (%)	Tail of the spiral casing (%)	Outlet (%)
MRFO-BP identification rate	85.389	98.833	96.056	100.000

(a)

(b)

Figure 15: Continued.

Classification results of vibration signals

(c)

Classification results of vibration signals
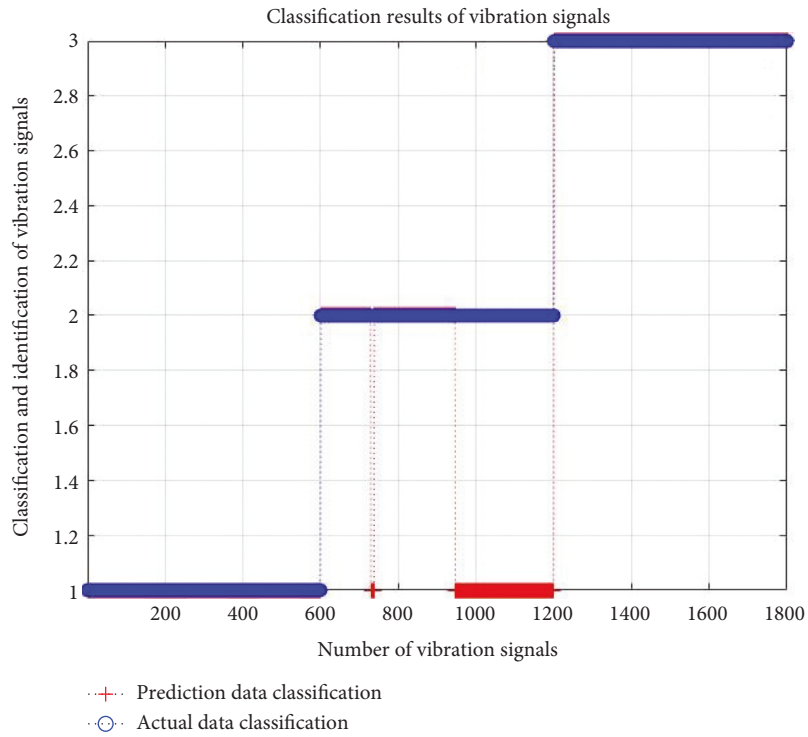
(d)

FIGURE 15: Identification rates of three units based on MRFO-BP neural network. (a) Generator; (b) middle of the spiral casing; (c) tail of the spiral casing; (d) outlet.
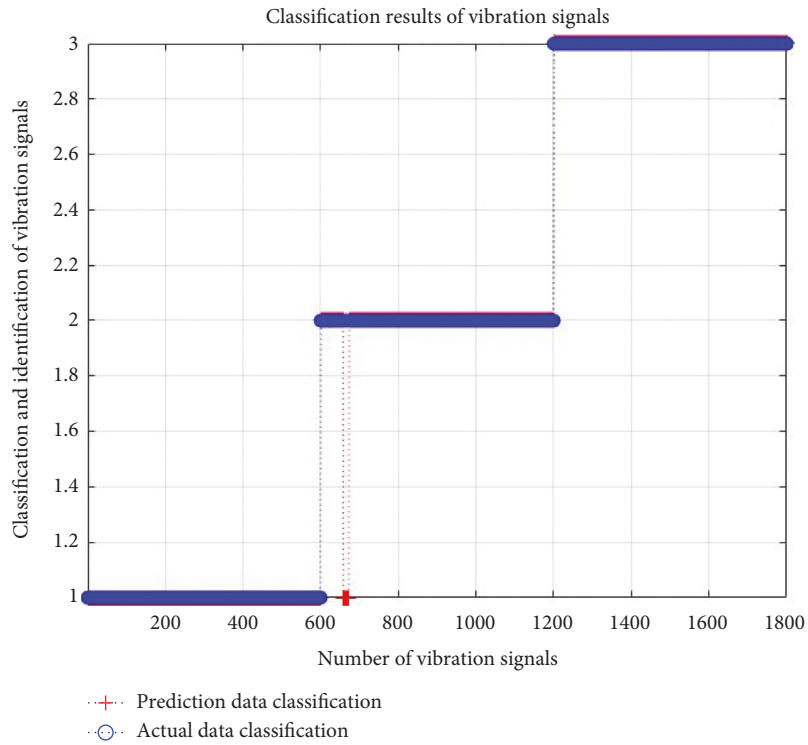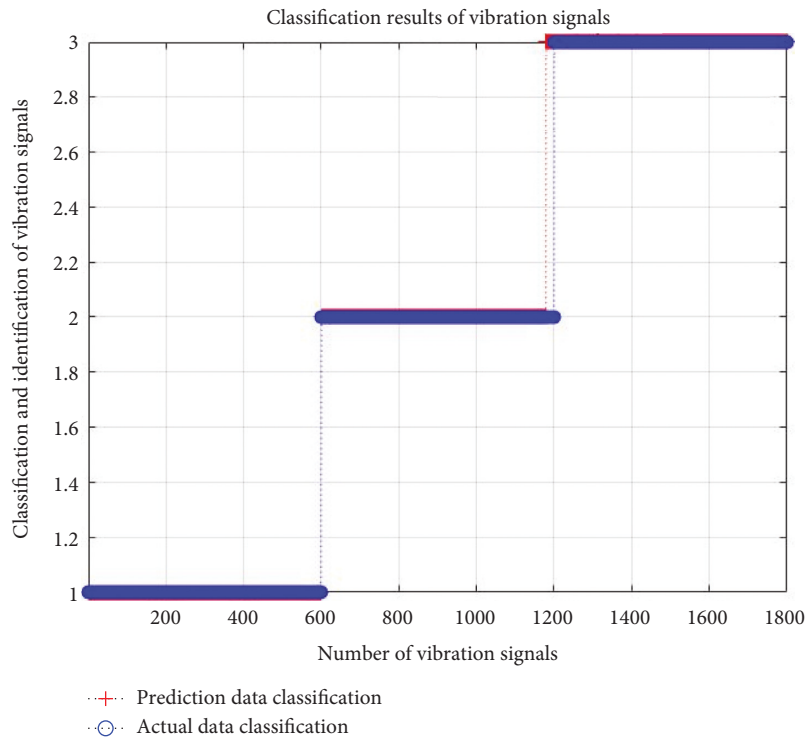
TABLE 4: Identification rates of three units based on BP neural network.

Measuring point position	Generator (%)	Inlet (%)	Middle of the spiral casing (%)	Tail of the spiral casing (%)	Outlet (%)
BP identification rate	68.278	90.278	87.722	88.222	88.611

Classification results of vibration signals

Number of vibration signals

....+.. Prediction data classification
..⊙.. Actual data classification

(a)

Classification results of vibration signals

Number of vibration signals

....+.. Prediction data classification
..⊙.. Actual data classification

(b)

Figure 16: Continued.

Classification results of vibration signals

···+·· Prediction data classification
···⊙·· Actual data classification

(c)

Classification results of vibration signals

···+·· Prediction data classification
···⊙·· Actual data classification

(d)

FIGURE 16: Continued.

Classification results of vibration signals

(e)

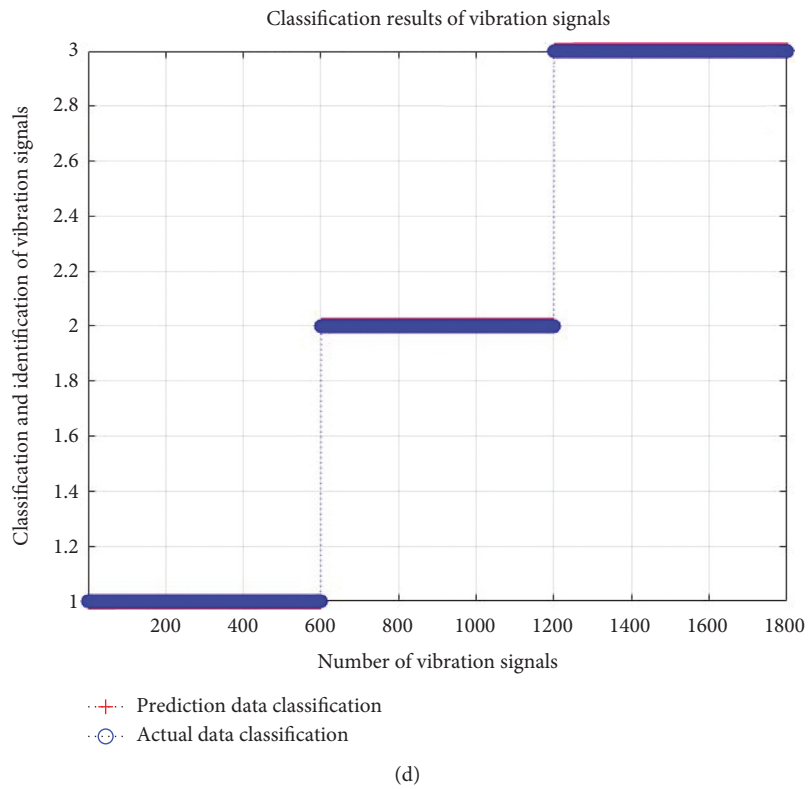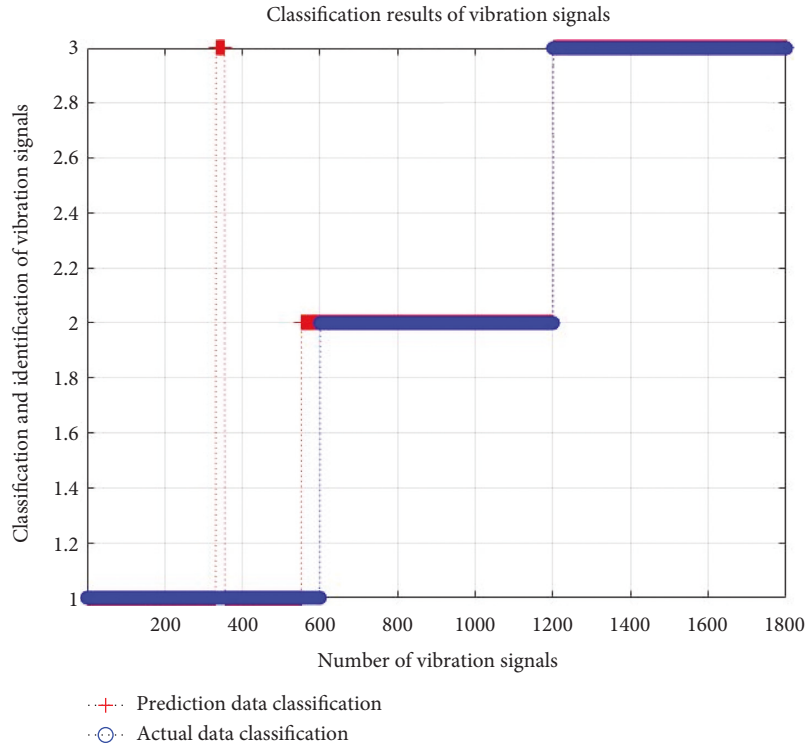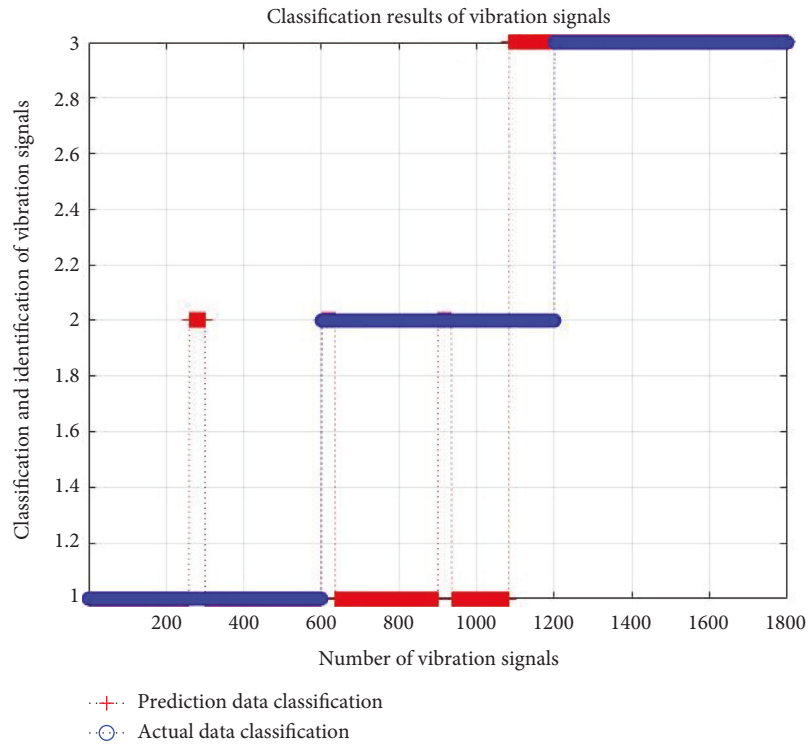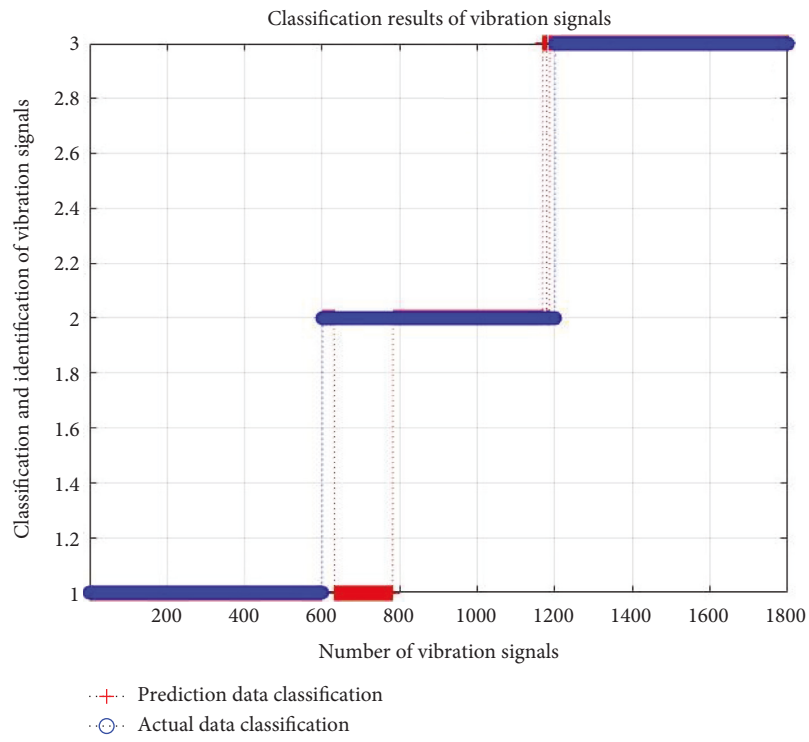FIGURE 16: Identification rates of three units based on BP neural network. (a) Generator; (b) inlet; (c) middle of the spiral casing; (d) tail of the spiral casing; (e) outlet.

TABLE 5: Identification rates of three units based on PSO-BP neural network.

Measuring point position	Generator (%)	Inlet (%)	Middle of the spiral casing (%)	Tail of the spiral casing (%)	Outlet (%)
PSO-BP identification rate	74.444	94.667	92.389	90.500	93.889

Based on the MRFO-BP neural network, the vibration signals of the four measuring points of the three units are trained and predicted, respectively. The obtained identification rates are shown in Table 3, and the identification rate images are shown in Figure 15. The four measuring points are the generator, the middle of the spiral casing, the tail of the spiral casing, and the outlet.

In Figure 15, at the generator, the 600 predicted values of the 1# unit completely coincide with marker 1, the 600 predicted values of the 4# unit completely coincide with marker 3, and the probability that the 600 predicted values of the 3# unit do not coincide with marker 2 is 14.611%. In the middle of the spiral casing, the 600 predicted values of the 1# unit completely coincide with marker 1, the 600 predicted values of the 4# unit completely coincide with marker 3, and the probability that the 600 predicted values of the 3# unit do not coincide with marker 2 is 1.167%. In the tail of the spiral casing, the 600 predicted values of the 3# unit completely coincide with marker 2, the 600 predicted values of the 4# unit completely coincide with marker 3, and the probability that the 600 predicted values of the 1# unit do not coincide with marker 1 is 3.944%. At the outlet, the 600 predicted values of the 1# unit completely coincide with marker 1, the 600

predicted values of the 3# unit completely coincide with marker 2, and the 600 predicted values of the 4# unit completely coincide with marker 3. Therefore, except for the generator, the average probability that the predicted values of other measuring points do not coincide with the classification markers is 1.981%.

4. Algorithm Comparison

In order to further verify the superiority of the MRFO-BP neural network, it is compared with PSO-BP neural network, BA-BP neural network, and BP neural network, respectively.

4.1. BP Neural Network Identification. The same data set is directly input into the BP neural network. At the same time, it is initialized according to the parameter settings of the MRFO-BP neural network. The identification rates of the three units at each measuring point are shown in Table 4, and the identification rate images are shown in Figure 16.

In Figure 16, at the generator, the 600 predicted values of the 4# unit completely coincide with marker 3, and the probability that the 600 predicted values of the 1# unit and the 3# unit, respectively, do not coincide with marker

(a)

(b)

Figure 17: Continued.

(c)

(d)

FIGURE 17: Continued.
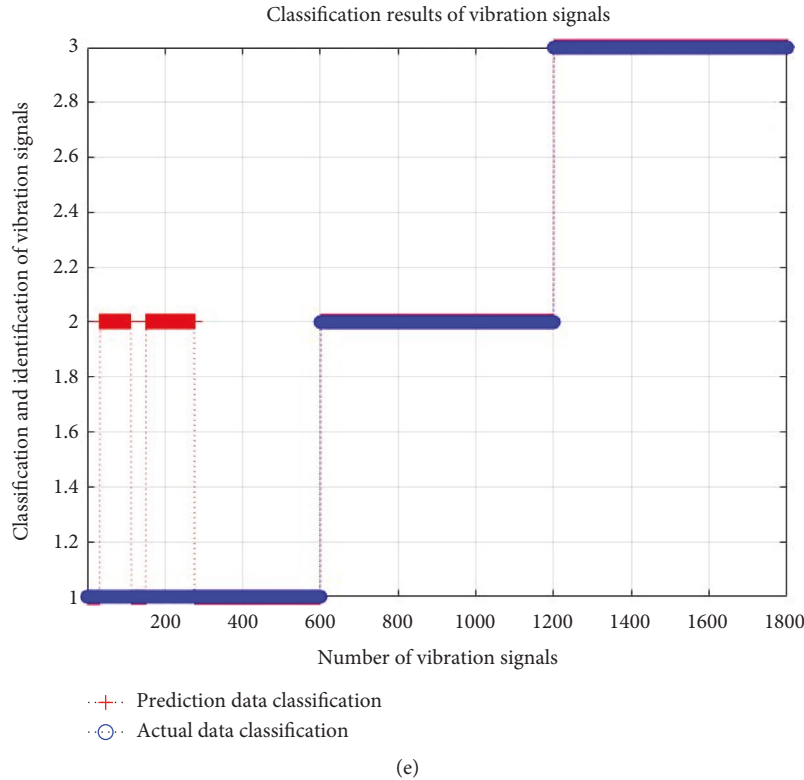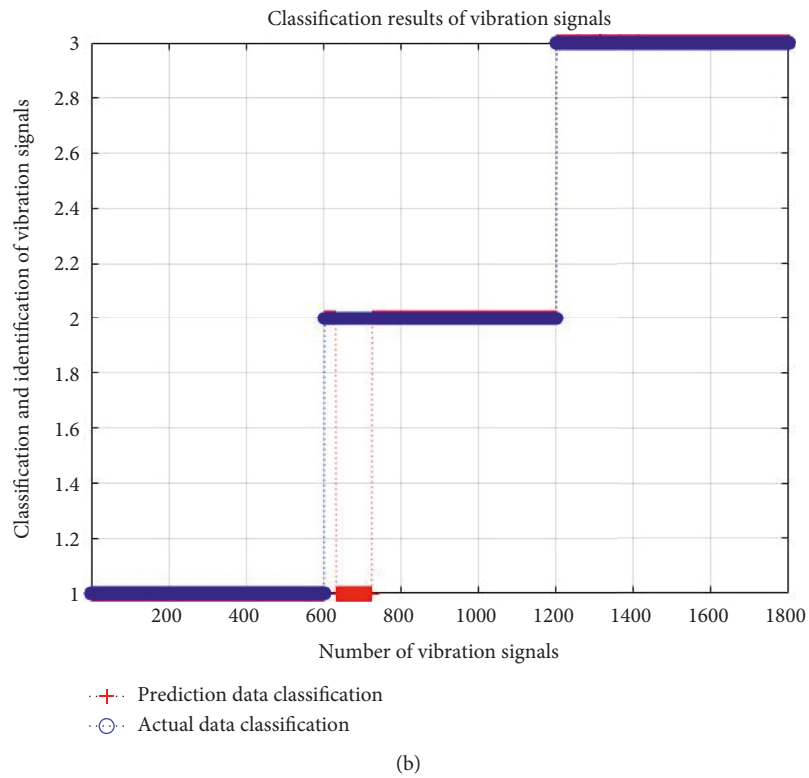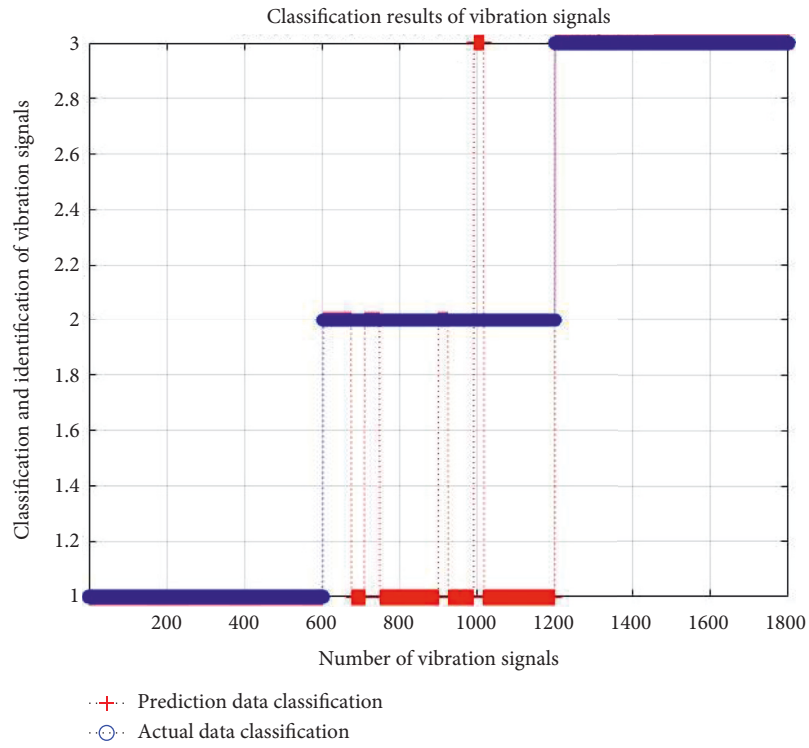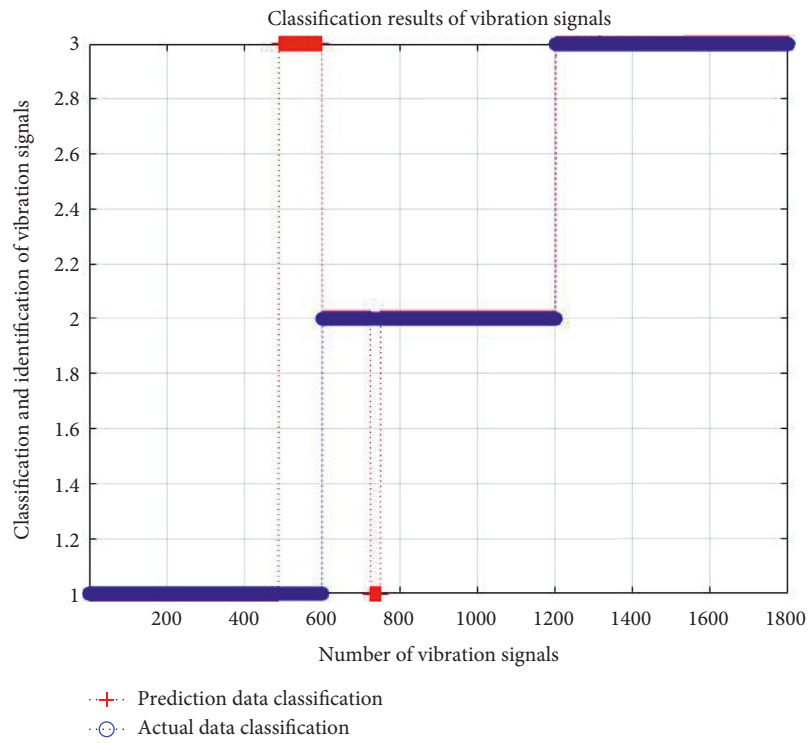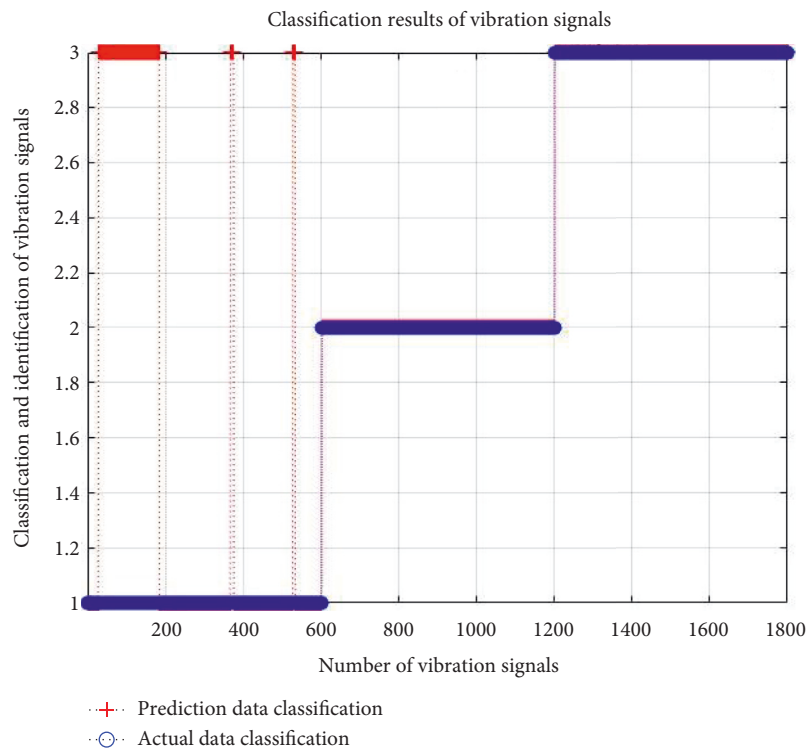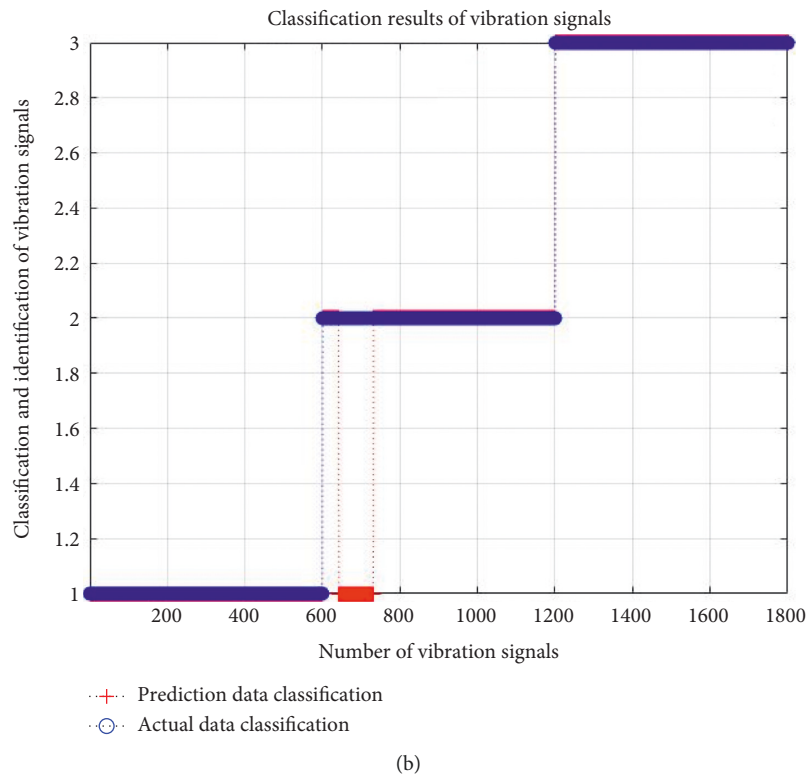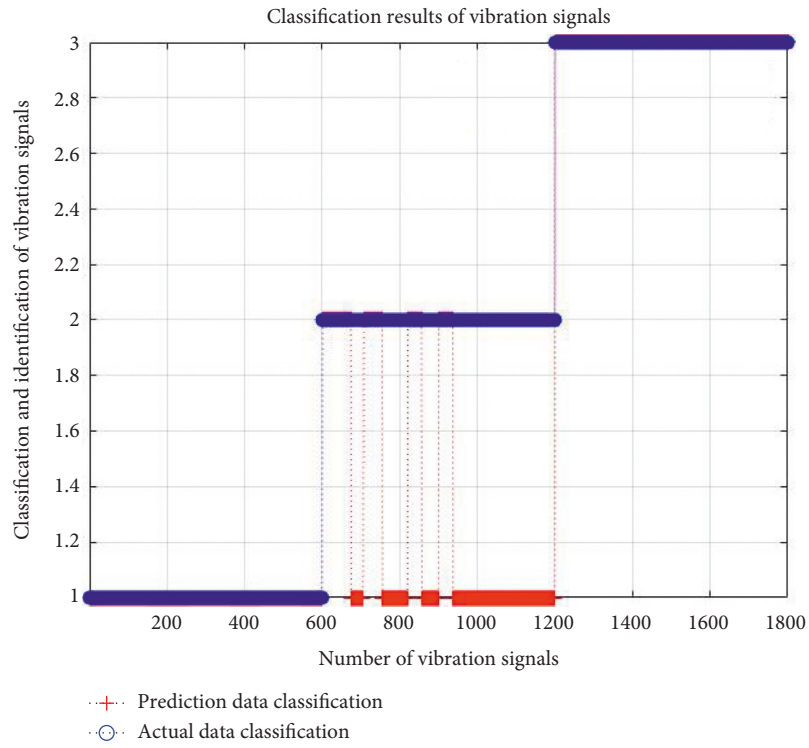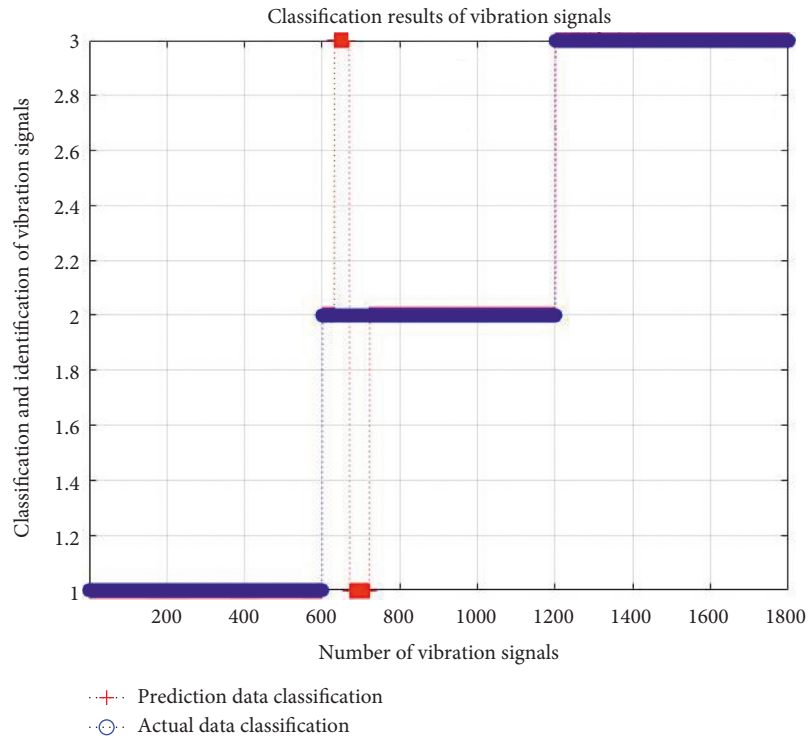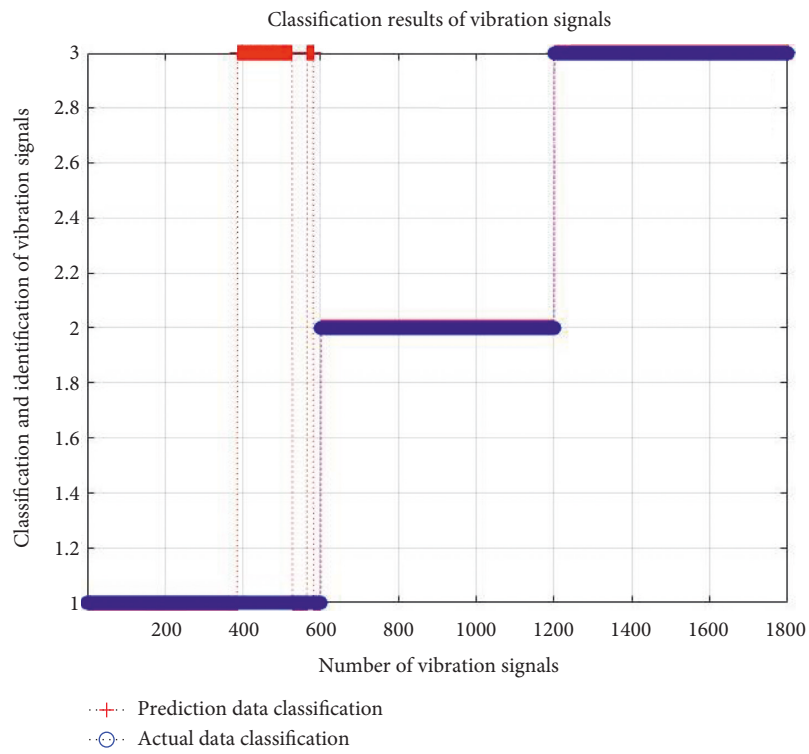
Classification results of vibration signals

(e)

FIGURE 17: Identification rates of three units based on PSO-BP neural network. (a) Generator; (b) inlet; (c) middle of the spiral casing; (d) tail of the spiral casing; (e) outlet.

TABLE 6: Identification rates of three units based on BA-BP neural network.

Measuring point position	Generator (%)	Inlet (%)	Middle of the spiral casing (%)	Tail of the spiral casing (%)	Outlet (%)
BA-BP identification rate	77.556	95.000	94.944	91.278	94.389

1 and marker 2 is 31.722%. At the inlet, the 600 predicted values of the 1# unit completely coincide with marker 1, the 600 predicted values of the 4# unit completely coincide with marker 3, and the probability that the 600 predicted values of the 3# unit do not coincide with marker 2 is 9.722%. In the middle of the spiral casing, the 600 predicted values of the 1# unit completely coincide with marker 1, the 600 predicted values of the 4# unit completely coincide with marker 3, and the probability that the 600 predicted values of the 3# unit do not coincide with marker 2 is 12.278%. In the tail of the spiral casing, the 600 predicted values of the 3# unit completely coincide with marker 2, the 600 predicted values of the 4# unit completely coincide with marker 3, and the probability that the 600 predicted values of the 1# unit do not coincide with marker 1 is 11.778%. At the outlet, the 600 predicted values of the 3# unit completely coincide with marker 2, the 600 predicted values of the 4# unit completely coincide with marker 3, and the probability that the 600 predicted values of the 1# unit do not coincide with marker 1 is 11.389%. Therefore, except for the generator, the average probability that the predicted values of other measuring points do not coincide with the classification markers is 11.292%.

4.2. PSO-BP Neural Network Identification. The PSO-BP neural network uses particle swarm algorithm (PSO) to optimize the BP neural network. The same data set is input into the PSO-BP neural network. At the same time, it is initialized according to the parameter settings of the MRFO-BP neural network. Through optimization, training, and prediction, the obtained prediction results are compared with each group of category labels. The obtained vibration signal identification rates of the three units at each measuring point are shown in Table 5, and the identification rate images are shown in Figure 17.

In Figure 17, at the generator, the 600 predicted values of the 1# unit completely coincide with marker 1, the 600 predicted values of the 4# unit completely coincide with marker 3, and the probability that the 600 predicted values of the 3# unit do not coincide with marker 2 is 25.556%. At the inlet, the 600 predicted values of the 1# unit completely coincide with marker 1, the 600 predicted values of the 4# unit completely coincide with marker 3, and the probability that the 600 predicted values of the 3# unit do not coincide with marker 2 is 5.333%. In the middle of the spiral casing, the 600 predicted values of the 4# unit completely coincide with marker 3, and the probability that the 600 predicted values of the 1# unit and the 3# unit,

(a)

(b)

Figure 18: Continued.

Classification results of vibration signals

(c)

Classification results of vibration signals
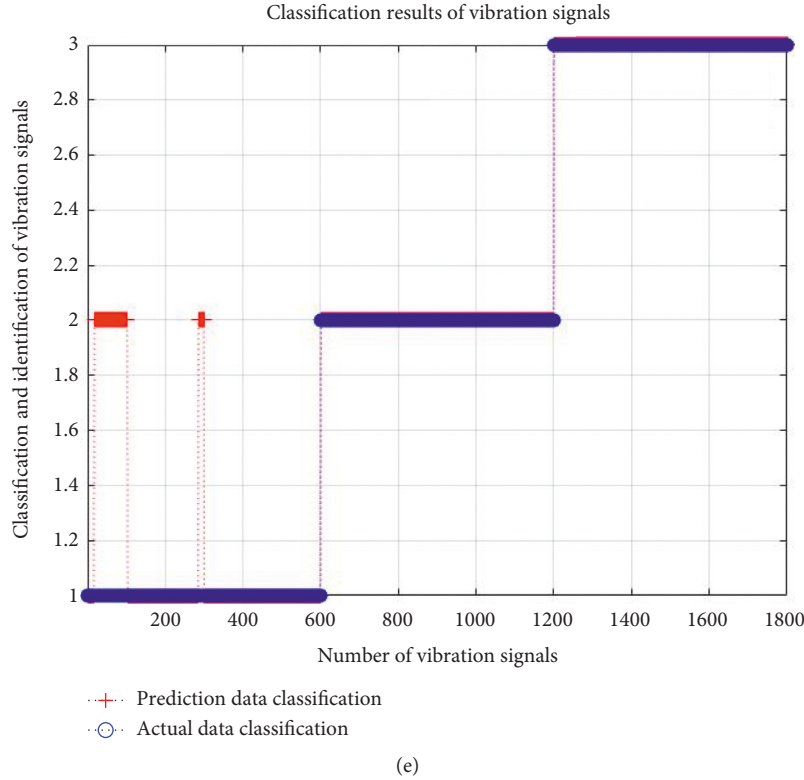

(d)

FIGURE 18: Continued.

FIGURE 18: Identification rates of three units based on BA-BP neural network. (a) Generator; (b) inlet; (c) middle of the spiral casing; (d) tail of the spiral casing; (e) outlet.

TABLE 7: Identification rates of three units based on four kinds of neural networks.

Measuring point position	Generator (%)	Inlet (%)	Middle of the spiral casing (%)	Tail of the spiral casing (%)	Outlet (%)
MRFO-BP identification rate	85.389	99.167	98.833	96.056	100.000
PSO-BP identification rate	74.444	94.667	92.389	90.500	93.889
BA-BP identification rate	77.556	95.000	94.944	91.278	94.389
BP identification rate	68.278	90.278	87.722	88.222	88.611

respectively, do not coincide with marker 1 and marker 2 is 7.611%. In the tail of the spiral casing, the 600 predicted values of the 3# unit completely coincide with marker 2, the 600 predicted values of the 4# unit completely coincide with marker 3, and the probability that the 600 predicted values of the 1# unit do not coincide with marker 1 is 9.500%. At the outlet, the 600 predicted values of the 3# unit completely coincide with marker 2, the 600 predicted values of the 4# unit completely coincide with marker 3, and the probability that the 600 predicted values of the 1# unit do not coincide with marker 1 is 6.111%. Therefore, except for the generator, the average probability that the predicted values of other measuring points do not coincide with the classification marks is 7.139%.

4.3. BA-BP Neural Network Identification. The BA-BP neural network uses Bat algorithm (BA) to optimize the BP neural network. The same data set is input into the BA-BP neural network. At the same time, it is initialized according to the parameter settings of the MRFO-BP neural network. Through optimization, training, and prediction, the obtained prediction results are compared with each group of category labels. The obtained vibration signal identification rates of the three units at each measuring point are shown in Table 6, and the identification rate images are shown in Figure 18.

In Figure 18, at the generator, the 600 predicted values of the 1# unit completely coincide with marker 1, the 600 predicted values of the 4# unit completely coincide with marker 3, and the probability that the 600 predicted values of the 3# unit do not coincide with marker 2 is 22.444%. At the inlet, the 600 predicted values of the 1# unit completely coincide with marker 1, the 600 predicted values of the 4# unit completely coincide with marker 3, and the probability that the 600 predicted values of the 3# unit do not coincide with marker 2 is 5.000%. In the middle of the spiral casing, the 600 predicted values of the 1# unit completely coincide with marker 1, the 600 predicted values of the 4# unit completely coincide with marker 3, and the probability that the 600 predicted values of the 3# unit do not coincide with
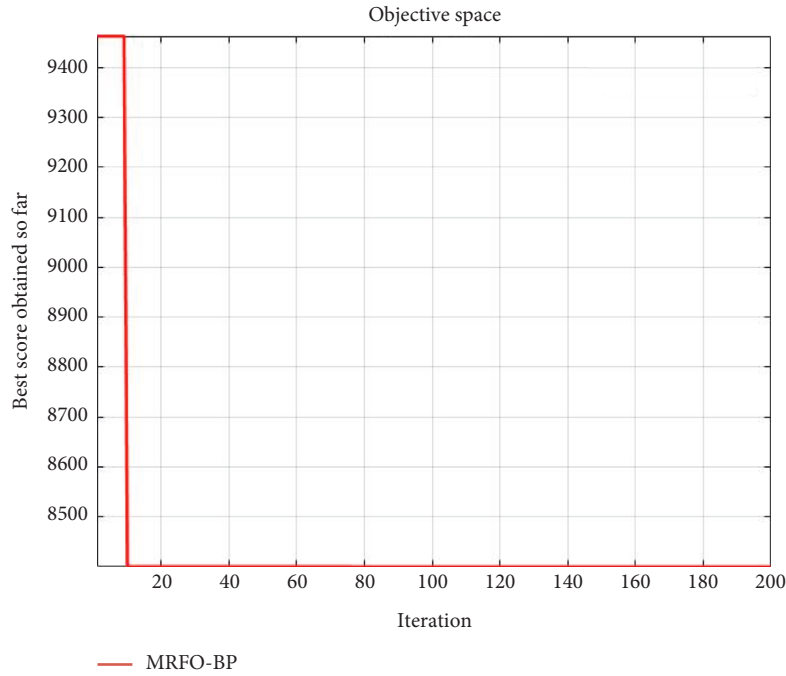
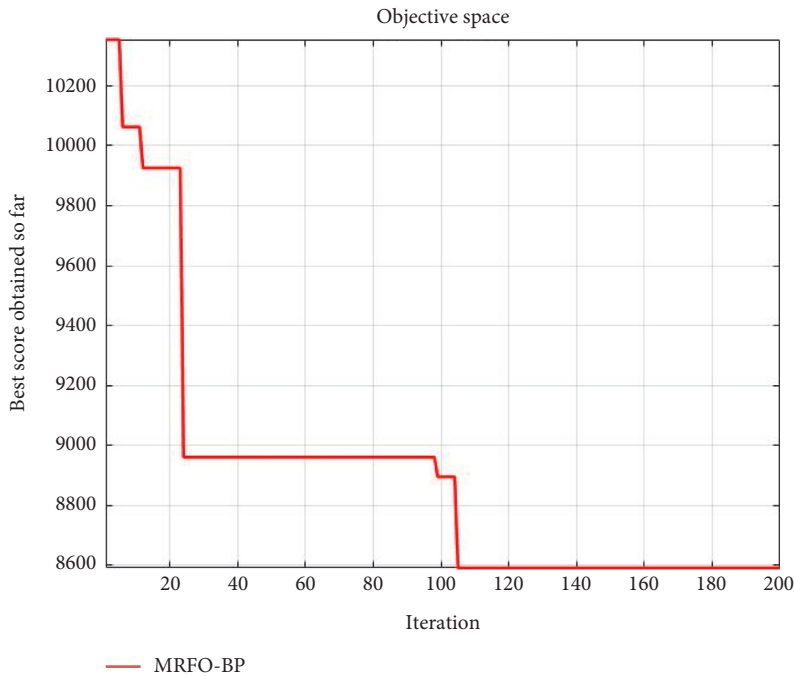FIGURE 19: Historical optimal position curve of the generator (comparative experiment).

FIGURE 20: Historical optimal position curve of the inlet (comparative experiment).

marker 2 is 5.056%. In the tail of the spiral casing, the 600 predicted values of the 3# unit completely coincide with marker 2, the 600 predicted values of the 4# unit completely coincide with marker 3, and the probability that the 600 predicted values of the 1# unit do not coincide with marker 1 is 8.722%. At the outlet, the 600 predicted values of the 3#

unit completely coincide with marker 2, the 600 predicted values of the 4# unit completely coincide with marker 3, and the probability that the 600 predicted values of the 1# unit do not coincide with marker 1 is 5.611%. Therefore, except for the generator, the average probability that the predicted
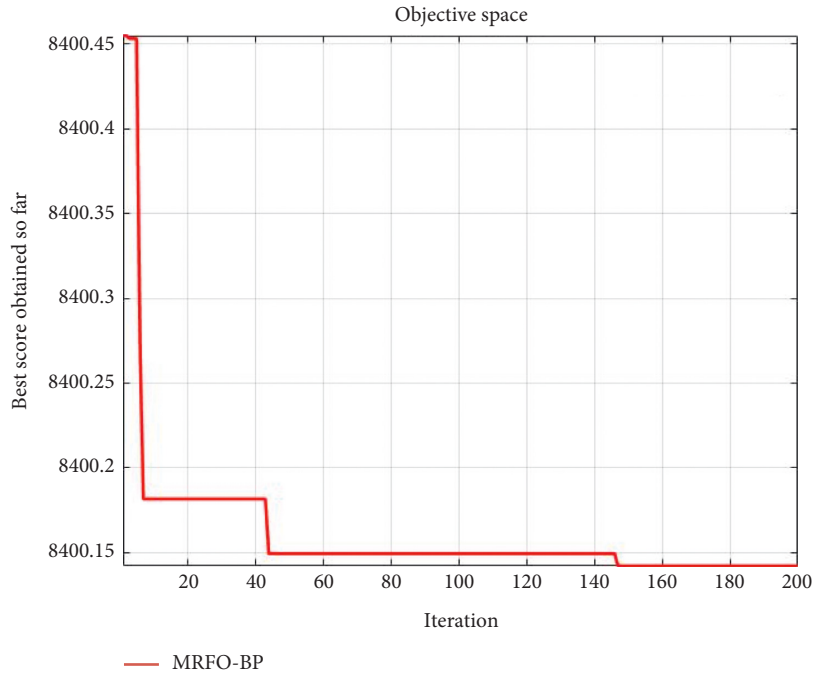
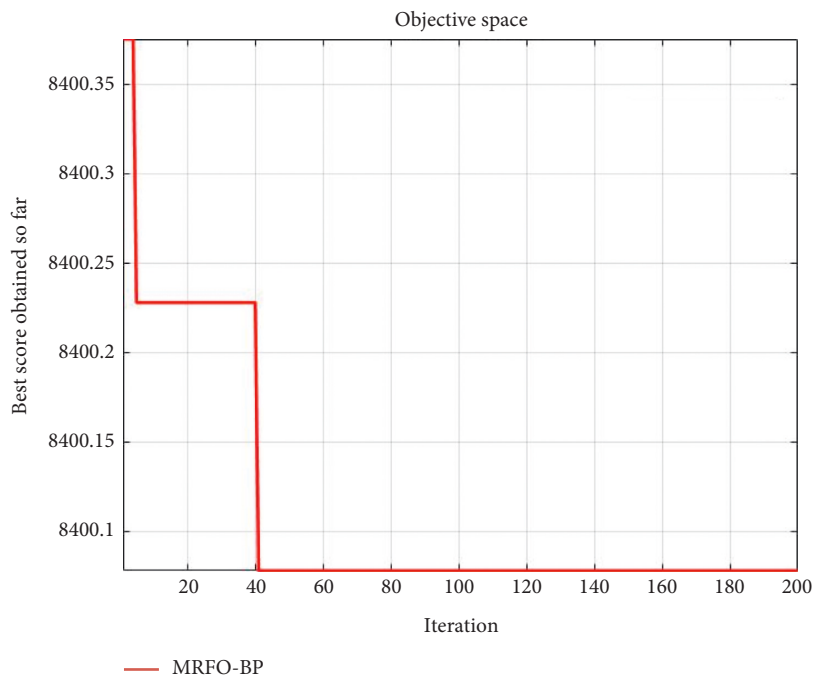FIGURE 21: Historical optimal position curve of the middle of the spiral casing (comparative experiment).

FIGURE 22: Historical optimal position curve of the tail of the spiral casing (comparative experiment).

values of other measuring points do not coincide with the classification markers is 6.097%.

The PSO-BP neural network, BA-BP neural network, and BP neural network are compared with MRFO-BP neural network. The vibration signal identification rates of three units in each measuring point of four neural networks are shown in Table 7.

According to the comparison in Table 7, although the identification rate of the vibration signals of the three units at the generator is lower than that of other measuring points, the identification rate of each measuring point of MRFO-BP neural network is greatly improved, which is much higher than that of the PSO-BP neural network, the BA-BP neural network, and the BP neural network. The analysis shows that the MRFO-BP neural network has obvious advantages in the
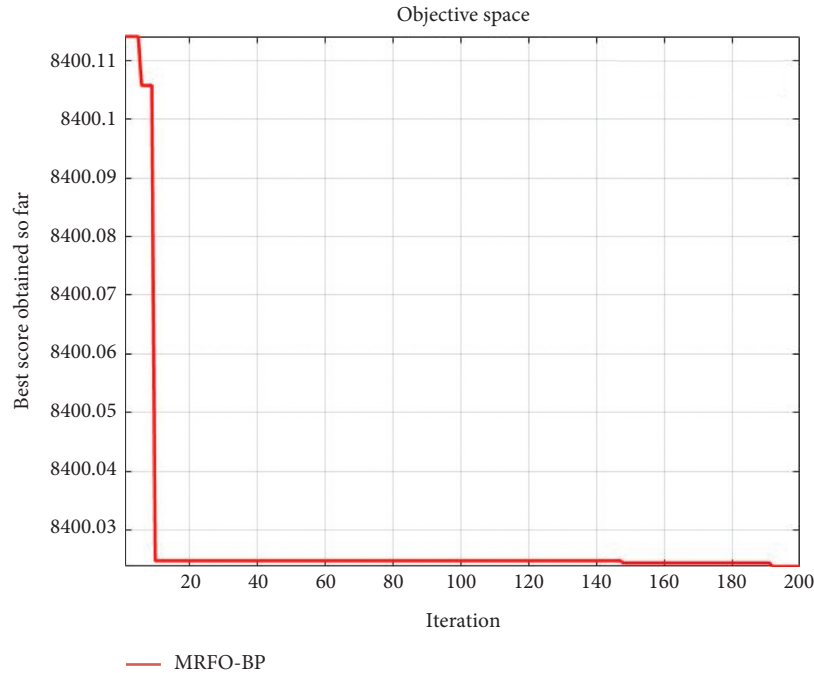
FIGURE 23: Historical optimal position curve of the outlet (comparative experiment).

TABLE 8: Identification rates of three units based on MRFO-BP neural network (comparative experiment).

Measuring point position	Generator (%)	Inlet (%)	Middle of the spiral casing (%)	Tail of the spiral casing (%)	Outlet (%)
MRFO-BP identification rate	85.722	98.500	96.833	95.778	98.611

identification of vibration signals of the residual pressure utilization hydraulic units.

5. Comparative Experiment

For the comparative experiment, 1# and 3# units with a guide vane opening of 30 mm and 4# unit with a guide vane opening of 33 mm were selected. Except for the different data of the unit used, the classification, processing, training, and identification of the data are the same as those of the unit with a guide vane opening of 40 mm.

5.1. Training MRFO-BP Neural Network. In the comparative experiment, the wavelet threshold denoising method is used to denoise the vibration signal, and EEMD method is used to extract the features of the denoised signal. IMF7-IMF12 are selected as the feature vector $X = [X_1, X_2, X_3, X_4, X_5, X_6]$ of each group of vibration signals.

The parameters of MRFO-BP neural network are initialized: the initial population number is 30, the maximum number of iterations is 200, the number of nodes in the input layer is 6, the number of nodes in the hidden layer is 10, and the number of nodes in the output layer is 3.

Six groups of signals from three units at each measuring point, each with 1000 IMF7-IMF12 components, are selected as the feature vectors of the vibration signals of residual pressure utilization hydraulic units. For each group of signals, the first 700 pieces of data are selected as training data, and the remaining 300 pieces of data are selected as the test data. The data are normalized, and the training data set and initialization parameters are input into the MRFO-BP neural network. After the BP neural network training and MRFO algorithm optimization, the optimal population and global optimal fitness value are obtained. The historical optimal fitness value curve of each measuring point in the target space is shown in Figures 19–23. The five measuring points are the generator, the inlet, the middle of the spiral casing, the tail of the spiral casing, and the outlet.

It can be seen from Figure 19 that the initial fitness value at the generator of the unit is 9462.632, which is maintained until the 9th iteration. The changes of the fitness value in the intermediate iteration process are as follows: the 10th to 76th iterations are 8400.241, the 77th to 80th iterations are 8400.217, and the 81st to 114th iterations are 8400.105. At the 115th iteration, the optimal fitness value is 8400.085.

It can be seen from Figure 20 that the initial fitness value at the inlet of the unit is 10353.948, which is maintained until the 5th iteration. The changes of the fitness value in the intermediate iteration process are as follows: the 6th to 11th iterations are 10062.538, the 12th to 23rd iterations are 9925.532, the 24th to 98th iterations are 8961.488, and the 99th to 104th iterations are 8895.809. At the 180th iteration, the optimal fitness value is 8591.741.

It can be seen from Figure 21 that the initial fitness value in the middle of the spiral casing of the unit is 8400.455, which is maintained until the second iteration. The changes
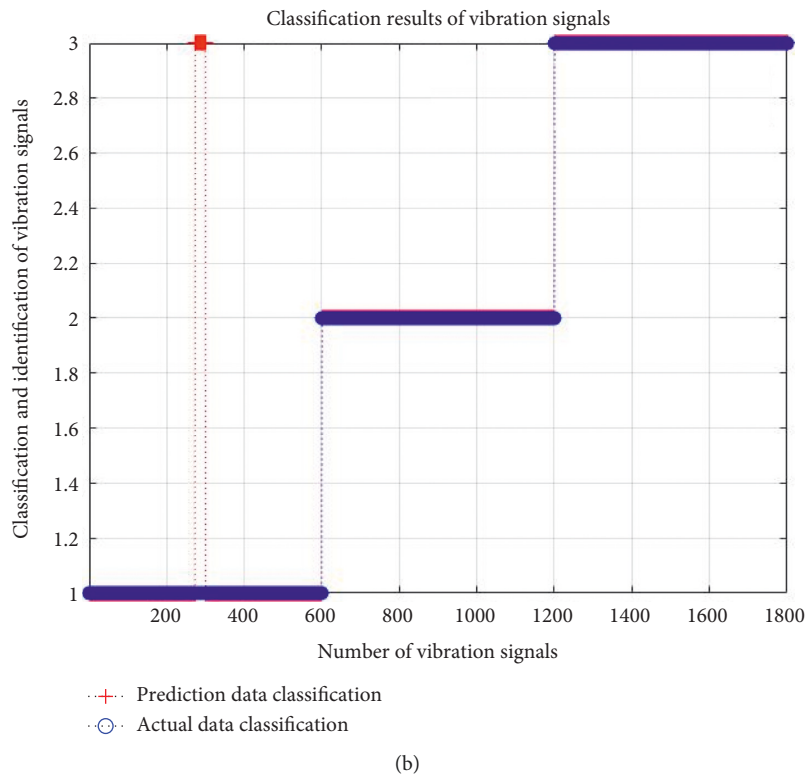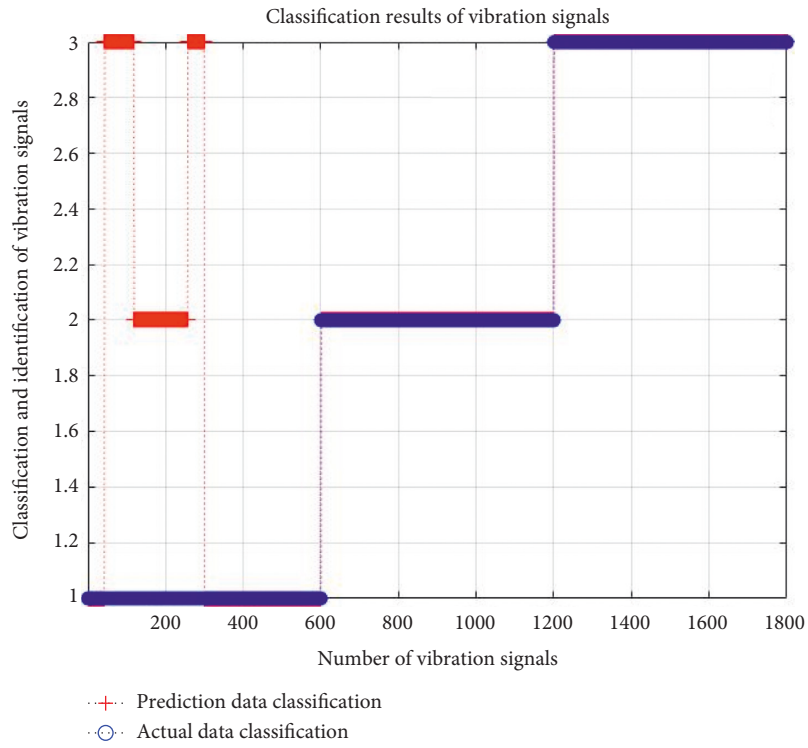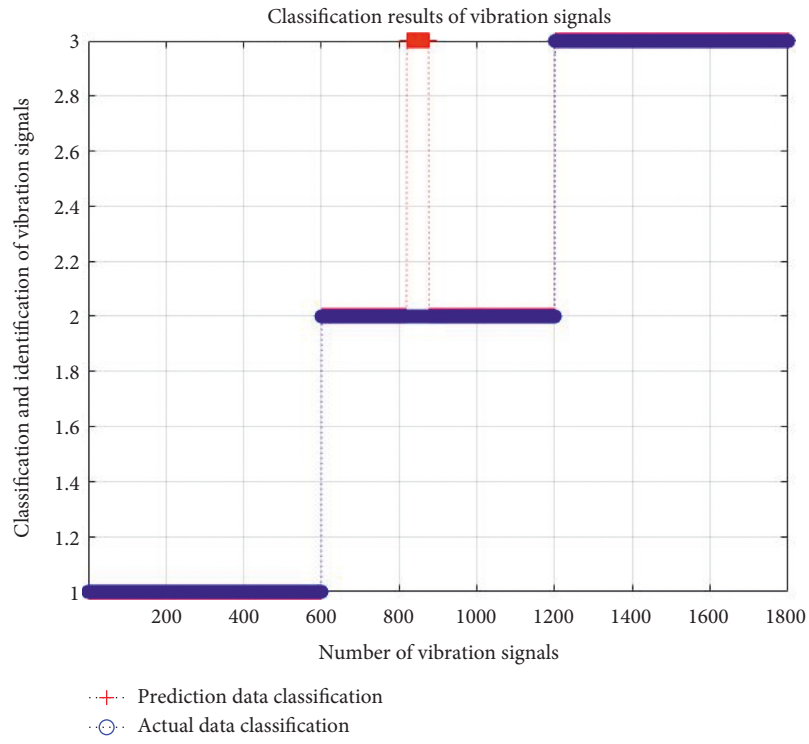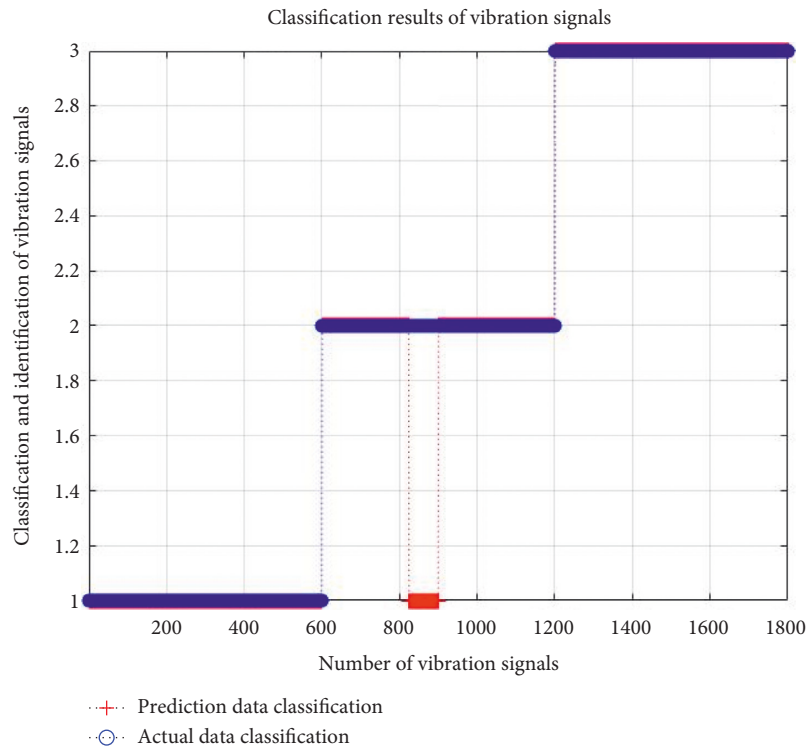
(a)

(b)

Figure 24: Continued.

Classification results of vibration signals

(c)

Classification results of vibration signals
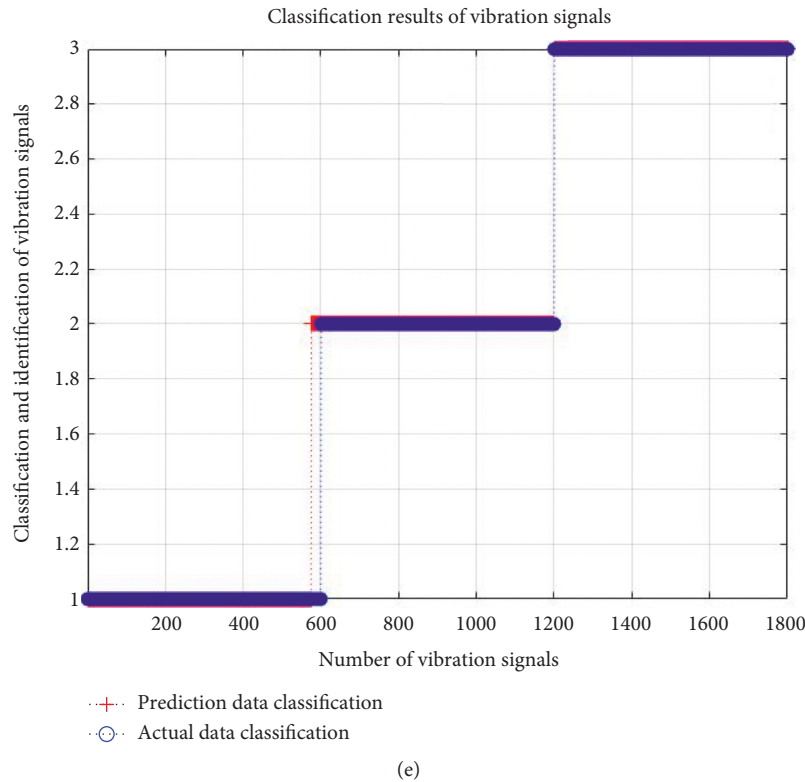

(d)

Figure 24: Continued.

(e)

FIGURE 24: Identification rates of three units based on MRFO-BP neural network. (a) Generator; (b) inlet; (c) middle of the spiral casing; (d) tail of the spiral casing; (e) outlet (comparative experiment).

of the fitness value in the intermediate iteration process are as follows: the 3rd to 5th iterations are 8400.453, the 6th iteration is 8400.276, the 7th to 43rd iterations are 8400.182, and the 44th to 146th iterations are 8400.149. At the 147th iteration, the optimal fitness value is 8400.142.

It can be seen from Figure 22 that the initial fitness value in the tail of the spiral casing of the unit is 8400.375, which is maintained until the 4th iteration. The fitness value is 8400.228 from the 5th to the 40th iteration. At the 41st iteration, the optimal fitness value is 8400.078.

It can be seen from Figure 23 that the initial fitness value at the outlet of the unit is 8475.034, which is maintained until the 5th iteration. The changes of the fitness value in the intermediate iteration process are as follows: the 6th to 9th iterations are 8400.106, the 10th to 147th iterations are 8400.025, and the 148th to 191st iterations are 8400.0244. At the 192nd iteration, the optimal fitness value is 8400.0238.

5.2. MRFO-BP Neural Network Identification. In the comparative experiment, the weights and thresholds of the BP neural network are optimized by using the optimal population. Then, the training data sets and test data sets of the three units at each measuring point are, respectively, input into the BP neural network. After training and prediction, the identification rates of vibration signals are obtained through comparing the prediction results with each group of classification labels. In the MRFO-BP neural network, the

identification rates of the three units at each measuring point are shown in Table 8, and the identification rate images are shown in Figure 24.

In Figure 24, at the generator, the 600 predicted values of the 3# unit completely coincide with marker 2, the 600 predicted values of the 4# unit completely coincide with marker 3, and the probability that the 600 predicted values of the 1# unit do not coincide with marker 1 is 14.278%. At the inlet, the 600 predicted values of the 3# unit completely coincide with marker 2, the 600 predicted values of the 4# unit completely coincide with marker 3, and the probability that the 600 predicted values of the 1# unit do not coincide with marker 1 is 1.5%. In the middle of the spiral casing, the 600 predicted values of the 1# unit completely coincide with marker 1, the 600 predicted values of the 4# unit completely coincide with marker 3, and the probability that the 600 predicted values of the 3# unit do not coincide with marker 2 is 3.167%. In the tail of the spiral casing, the 600 predicted values of the 1# unit completely coincide with marker 1, the 600 predicted values of the 4# unit completely coincide with marker 3, and the probability that the 600 predicted values of the 3# unit do not coincide with marker 2 is 4.222%. At the outlet, the 600 predicted values of the 3# unit completely coincide with marker 2, the 600 predicted values of the 4# unit completely coincide with marker 3, and the probability that the 600 predicted values of the 1# unit do not coincide with marker 1 is 1.389%. Therefore, except for the generator, the average probability that the predicted values of other

TABLE 9: Identification rates of three units based on four kinds of neural networks (comparative experiment).

Measuring point position	Generator (%)	Inlet (%)	Middle of the spiral casing (%)	Tail of the spiral casing (%)	Outlet (%)
MRFO-BP identification rate	85.722	98.500	96.833	95.778	98.611
PSO-BP identification rate	77.611	94.000	93.278	92.944	92.056
BA-BP identification rate	81.944	94.667	93.500	92.278	94.500
BP identification rate	69.500	89.778	88.556	90.444	90.722

measuring points do not coincide with the classification markers is 2.570%.

5.3. Algorithm Comparison. The same data sets are input into BP neural network, PSO-BP neural network, and BA-BP neural network, respectively. At the same time, it is initialized according to the parameter settings of the MRFO-BP neural network. Through optimization, training, and prediction, the obtained prediction results are compared with each group of category labels. In each algorithm, the vibration signal identification rate of three units at each measuring point is obtained.

The PSO-BP neural network, BA-BP neural network, and BP neural network are compared with MRFO-BP neural network. The vibration signal identification rates of three units in each measuring point of four neural networks are shown in Table 9.

In the comparative experiment, it can be obtained from Table 9 that although the identification rate of the vibration signals of the three units at the generator is lower than that of other measuring points, the identification rate of each measuring point of MRFO-BP neural network is greatly improved, which is much higher than that of the PSO-BP neural network, the BA-BP neural network, and the BP neural network. The analysis shows that the MRFO-BP neural network has obvious advantages in the identification of vibration signals of the residual pressure utilization hydraulic units.

6. Conclusions

Combined with wavelet threshold denoising and EEMD decomposition, an analysis method based on MRFO-BP neural network is proposed for feature extraction and identification of vibration signals of residual pressure utilization hydraulic units. After the optimization, training, and identification of MRFO-BP neural network, combined with the results of the comparative experiment, the original experimental conclusions are as follows:

Wavelet threshold denoising and EEMD decomposition are performed on the vibration signals of the residual pressure utilization hydraulic unit collected on-site, and the feature vectors are extracted and constructed. The feature vector is input into the MRFO-BP neural network recognition model, and the identification rates of the three units at different measuring points are obtained. The average identification rate of other measuring points is 98.514%, except 85.389% at the generator.

The identification rates of MRFO-BP neural network are compared with PSO-BP neural network, BA-BP neural network, and BP neural network. The identification rate of

the MRFO-BP neural network at different measuring points: the identification rate of the generator is 85.389%, and the average identification rate of other measuring points is 98.514%. The identification rate of the PSO-BP neural network at different measuring points: the identification rate of the generator is 74.444%, and the average identification rate of other measuring points is 92.861%. The identification rate of the BA-BP neural network at different measuring points: the identification rate of the generator is 77.556%, and the average identification rate of other measuring points is 93.903%. The identification rate of the BP neural network at different measuring points: the identification rate of the generator is 68.278%, and the average identification rate of other measuring points is 88.708%. It can be concluded that the MRFO-BP neural network has higher identification accuracy, except that the lifting amplitude of generator is 10.945% (PSO-BP), 7.833% (BA-BP), and 17.111% (BP neural network), and the average lifting amplitude of other measuring points is 5.653% (PSO-BP) and 4.611%, respectively. Therefore, the identification accuracy of vibration signals of residual pressure utilization hydraulic units obtained by MRFO-BP neural network is significantly improved.

Data Availability

The data are derived from field experiments and involves confidentiality so are not shared.

Conflicts of Interest

The authors declare that there are no conflicts of interest regarding the publication of this paper.

Acknowledgments

References

[1] N. Lu, G. T. Zhang, F. X. Liu, T. X. Zhou, and H. G. Bian, "Research on vibration fault diagnosis method of hydropower unit based on LTSA and spectral clustering," *Engineering Journal of Wuhan University*, vol. 54, no. 11, pp. 1064–1069, 2021.

[2] X. Hu, Z. H. Xiao, and D. Liu, "Vibration fault identification method of hydropower unit based on EEMD-SDCC I-HMM,"

Journal of Vibration and Shock, vol. 41, no. 03, pp. 165–175+230, 2022.

[3] S. Han, N. Mannan, D. C. Stein, K. R. Pattipati, and G. M. Bollas, "Classification and regression models of audio and vibration signals for machine state monitoring in precision machining systems," *Journal of Manufacturing Systems*, vol. 61, pp. 45–53, 2021.

[4] Y. Li, B. Tang, X. Jiang, and Y. Yi, "bearing fault feature extraction method based on GA-VMD and center frequency," *Mathematical Problems in Engineering*, vol. 2022, pp. 1–19, 2022.

[5] Y. Li, L. Mu, and P. Gao, "Particle swarm optimization fractional slope entropy: a new time series complexity indicator for bearing fault diagnosis," *Fractal and Fractional*, vol. 6, no. 7, p. 345, 2022.

[6] W. Qiang, H. Cui, Y. Xie, X. Q. Qu, and L Xu, "A study on feature extraction and recognition of fatigue crack AE signals of oil and gas pipelines in offshore platforms," *Journal of Vibration and Shock*, vol. 40, no. 8, pp. 70–78, 2021.

[7] Y. Hou, A. O Yang, W. Guo, D. Zhang, and S. Shi, "Short-term power generation prediction using grey wolf optimization algorithm and neural network," *Journal of Shaanxi University of Science & Technology*, vol. 40, no. 04, pp. 171–177, 2022.

[8] B. Liu, R. Wang, G. Zhao et al., "Prediction of rock mass parameters in the TBM tunnel based on BP neural network integrated simulated annealing algorithm," *Tunnelling and Underground Space Technology*, vol. 95, Article ID 103103, 2019.

[9] C.-Y. Lee and Y.-H. Cheng, "motor fault detection using wavelet transform and improved PSO-BP neural network," *Processes*, vol. 8, no. 10, p. 1322, 2020.

[10] D. Deshwal, P. Sangwan, and D. Kumar, "A language identification system using hybrid features and back-propagation neural network," *Applied Acoustics*, vol. 164, Article ID 107289, 2020.

[11] E. H. Houssein, I. E. Ibrahim, N. Neggaz, M. Hassaballah, and Y. M. Wazery, "An efficient ECG arrhythmia classification method based on Manta ray foraging optimization," *Expert Systems with Applications*, vol. 181, Article ID 115131, 2021.

[12] D. Yousri, T. S. Babu, S. Mirjalili, N. Rajasekar, and M. A. Elaziz, "A novel objective function with artificial ecosystem-based optimization for relieving the mismatching power loss of large-scale photovoltaic array," *Energy Conversion and Management*, vol. 225, Article ID 113385, 2020.

[13] M. G. M. Abdolrasol, S. M. S. Hussain, T. S. Ustun et al., "Artificial neural networks based optimization techniques: a review," *Electronics*, vol. 10, no. 21, p. 2689, 2021.

[14] G. J. Xiong, J. Zhang, D. Y. Shi, and X. F. Yuan, "Application of supply-demand-based optimization for parameter extraction of solar photovoltaic models," *Complexity*, vol. 2019, pp. 1–22, 2019.

[15] E. E. Elattar, A. M. Shaheen, A. M. El-Sayed, R. A. El-Sehiemy, and A. R. Ginidi, "Optimal operation of auto-mated distribution networks based-MRFO algorithm," *IEEE Access*, vol. 9, pp. 19586–19601, 2021.

[16] M. A. Almagboul, F. Shu, Y. W. Qian, X. Zhou, J. Wang, and J. Hu, "Atom search optimization algorithm based hybrid antenna array receive beamforming to control sidelobe level and steering the null," *AEU-International Journal of Electronics and Communications*, vol. 111, Article ID 152854, 2019.

[17] Y. Zhang and Y. L. Liu, "A serial fault arc identification method based on PSO optimized BP neural network," *Transducer and Microsystem Technologies*, vol. 35, no. 7, pp. 22–25, 2016.

[18] A. Ismail, D.-S. Jeng, and L. L. Zhang, "An optimised product-unit neural network with a novel PSO-BP hybrid training algorithm: applications to load-deformation analysis of axially loaded piles," *Engineering Applications of Artificial Intelligence*, vol. 26, no. 10, pp. 2305–2314, 2013.

[19] Md. Shadman Abid, H. J. Apon, K. A. Morshed, and A. Ahmed, "Optimal planning of multiple renewable energy-integrated distribution system with uncertainties using artificial Hummingbird algorithm," *IEEE Access*, vol. 10, pp. 40716–40730, 2022.

[20] A. Tharwat, A. E. Hassanien, and B. E. Elnaghi, "A BA-based algorithm for parameter optimization of Support Vector Machine," *Pattern Recognition Letters*, vol. 93, pp. 13–22, 2017.

[21] X. Yang, M. Qiu, L. H. Chen, and Y. Chen, "Denoising method of vibration signals of rolling bearing based on adaptive wavelet threshold function of PSO-RWE," *Journal of Aerospace Power*, vol. 35, no. 11, pp. 2339–2347, 2020.

[22] I. Vamsi, M. P. Hemanth, P. Kumar Penumakala, and G. R. Sabareesh, "Damage monitoring of pultruded GFRP composites using wavelet transform of vibration signals," *Measurement*, vol. 2022, Article ID 111177, 2022.

[23] H. Kuang, R. L. Wang, J. Zhang, and J. Yan, "Research on suppression method of EMD endpoint effect based on SVM," *Computer Engineering and Applications*, vol. 51, no. 11, pp. 96–200+227, 2015.

[24] Z. H. Wu and N. E. Huang, "Ensemble empirical mode decomposition: a noise-assisted data analysis method," *Advances in Adaptive Data Analysis*, vol. 01, no. 01, pp. 1–41, 2009.

[25] C. F. Sun, *Research on Fault Signal Extraction and Fault Identification of Rolling Bearing of Vibrating Screen Vibrating Motor Based on Wavelet Analysis-EEMD-BSS and Improved KNN Algorithm*, Doctoral Thesis, Xi'an University of Architecture and Technology, vol. 36, no. 2, pp. 225–239, Xi'an, Shanxi, China, 2014.

[26] K. D. He, J. Chen, Y. Jin, W. J. Jiang, and Z. H. Xiao, "Application of EEMD multi-scale entropy and ELM in feature extraction of vibration signals of hydropower units," *China Rural Water and Hydropower*, vol. 05, pp. 176–182+187, 2021.

[27] S. Q. Feng, "Distribution network fault interval location based on manta ray foraging optimization algorithm," *Journal of Lanzhou University of Arts and Science (Natural Sciences)*, vol. 35, no. 01, pp. 19–23, 2021.

[28] F. R. Bi, T. Ma, and X. Wang, "Development of a novel knock characteristic detection method for gasoline engines based on wavelet-denoising and EMD decomposition," *Mechanical Systems and Signal Processing*, vol. 117, pp. 517–536, 2019.

[29] L. Li and S. S. Ni, "Fault diagnosis of shearer gearbox based on improved wavelet denoising preprocessing and EEMD," *Journal of Central South University*, vol. 47, no. 10, pp. 3394–3400, 2016.

[30] L. Zhao, G. Hong, Z. Wang et al., "Research on fault vibration signal features of GIS disconnector based on EEMD and kurtosis criterion," *IEEJ Transactions on Electrical and Electronic Engineering*, vol. 16, no. 5, pp. 677–686, 2021.

[31] Y. Dongyang, S. Fengchang, D. Xiaochuan, W. Zheng, W. Jiahua, and Z. Zhichao, "Wind speed time series forecasting method in wind farm based on EEMD," *IOP Conference Series: Earth and Environmental Science*, vol. 791, no. 1, Article ID 012140, 2021.

[32] X. B. Zhang, "Gearbox fault diagnosis method based on the fusion of EEMD and improved Elman-NN," *Vibroengineering, PROCEDIA*, vol. 36, pp. 24–29, 2021.

[33] W. G. Zhao, Z. X. Zhang, and L. Y. Wang, "Manta ray foraging optimization: An effective bio-inspired optimizer for engineering applications," *Engineering Applications of Artificial Intelligence*, vol. 87, pp. 103300.1–103300.25, 2020.

[34] J. H. Ye, F. Z. Luo, and L. Yang, "Topology identification of distribution network based on improved manta ray foraging optimization SVM," *Proceedings of the CSU-EPSA*, vol. 33, no. 10, pp. 43–50, 2021.

[35] J. M. Li, X. F. Yao, X. D. Wang, Q. W. Yu, and Y. G. Zhang, "Multiscale local features learning based on BP neural network for rolling bearing intelligent fault diagnosis," *Measurement*, vol. 153, Article ID 107419, 2020.

[36] J. F. Liu, B. Y. Dong, X. Yu, and H. B. Wan, "Fault diagnosis method of rolling bearing based on FSC-MPE and BP neural network," *Chinese Journal of Ship Research*, vol. 16, no. 06, pp. 183–190, 2021.